AIAA Aviation 2017, 5-9 June 2017

Jet-Surface Interaction Noise from High-Aspect Ratio Nozzles: Test Summary

Cliff Brown[*] and Gary Podboy[†]

NASA Glenn Research Center, Cleveland, OH, 44135, USA

Noise and flow data have been acquired for a 16:1 aspect ratio rectangular nozzle exhausting near a simple surface at the NASA Glenn Research Center as part of an ongoing effort to understand, model, and predict the noise produced by current and future concept aircraft employing a tightly integrated engine/airframe designs. The particular concept under consideration in this experiment is a blended-wing-body airframe powered by a series of electric fans exhausting through slot nozzle over an aft deck. The exhaust Mach number and surface length were parametrically varied during the test. Far-field noise data were acquired for all nozzle/surface geometries and exhaust flow conditions. Phased-array noise source localization data and in-flow pressure data were also acquired for a subset of the isolated (no surface) and surface configurations; these measurements provide data that have proven useful for modeling the jet-surface interaction noise source and the surface effect on the jet-mixing noise in round jets. A summary of the nozzle/surface geometry, flow conditions tested, and data collected are presented.

Nomenclature

$+$	add decibels (logarithmic))
β	nondimensional jet potential core length ($\beta = x_C/H_j$)
$\bigoplus$	add power (antilogarithmic)
$\gamma_{\theta 1,\theta 2}$	coherence between observers at angles θ_1 and θ_2
ϕ	observation angle relative to the nozzle minor axis (azimuthal or roll angle)
θ	observation angle relative to the upstream jet axis (polar or yaw angle)
A_j	nozzle area
c_a	speed of sound at ambient conditions
D_{eq}	round nozzle exit diameter with equivalent area, $D_{eq} = (4H_jW_j/\pi)^{1/2}$
f	frequency (Hz)
FPR	Fan Pressure Ratio
G_S	effect of surface on PSD_M, ΔdB
H_j	nozzle height
M_a	acoustic Mach number ($M_a = U_j/c_a$)
P_a	ambient pressure
$P_{t,j}$	total jet pressure
PSD	power spectral density relative 20μPa
PSD_D	power spectral density, jet-surface trailing edge source
PSD_M	power spectral density, jet-mixing noise source
PSD_T	total power spectral density, all sources and effects
St_{Deq}	Strouhal number using nozzle equivalent diameter ($St_{Deq} = fD_{eq}/U_j$)
St_{Hj}	Strouhal number using nozzle slot height ($St_{Hj} = fH_j/U_j$)
T_tR	jet total temperature ratio
U_j	jet exit velocity

---

[*] Research Engineer, Acoustics Branch, 21000 Brookpark Rd., AIAA Member.

[†] Research Engineer, Acoustics Branch, 21000 Brookpark Rd., AIAA Member

W_j	nozzle width
x_C	jet potential core length
x_E	axial distance from jet exit to surface trailing edge
y_E	surface span

I. Introduction

Many modern aircraft design concepts tightly couple the engine with the airframe to increase operational efficiency. However, these designs result in the high-speed engine exhaust passing near or directly over the aft airframe surfaces potentially increasing the noise produced. The push to high bypass ratio engines in traditional engine-under-wing applications, for example, has placed the exhaust flow close to the underside of the wing; any noise produced by this flow-surface interaction can be directly radiated to people on the ground. In contrast, some concept aircraft have moved the engine pods over the wing[1] or fuselage[2] so that the surfaces might shield ground observers from a portion of the engine noise produced. While some of these designs maintain a traditional engine-pylon architecture, other more futuristic concepts change the entire propulsion system in an effort to reduce noise.[3]

The NASA N3-X hybrid wing-body concept aircraft (Figure 1) uses a turbo-electric distributed propulsion (TeDP) system aimed at meeting emissions, performance, and noise goals for production aircraft three generations beyond the capabilities of the current fleet.[3–5] The TeDP system uses a row of electric fans embedded in the aft body to propel the aircraft. The TeDP system uses two turbine engines, located on the wingtips, to produce the electricity that powers the fans. Air is ingested through a high-aspect ratio inlet on the top side of the aircraft and exhausted through a similarly shaped nozzle before passing over the aft deck of the aircraft. The flow path is divided into channels so that each fan operates in isolation giving rise to septa in the exhaust nozzle. A system level assessment of the N3-X has shown that the concept has the potential to meet its noise targets.[5] However, this assessment used existing tools and methods that required considerable modifications for the unusual N3-X geometry. Therefore, a scale-model test of a high-aspect ratio exhaust nozzle with a simplified aft deck and septa has been conducted to provide far-field noise validation data. In addition, a more limited set of flow and noise source localization data were collected to provide insight into the noise sources and surface effects (e.g. noise shielding, jet-surface interaction noise). While the N3-X concept was the inspiration for this test, there are some notable differences, particularly nozzle aspect-ratio, dictated by the test facility and limitations of model scale. Even so, these data combine with results from previous tests using round[6–9] and lower aspect-ratio rectangular[10] nozzles to form a database suitable for developing and validating noise models and prediction tools for this class of aircraft. This paper will give a summary of the Jet-Surface Interaction Noise - High Aspect Ratio Nozzles test, present the resulting flow and noise data for future reference, and briefly discuss the implications of these model-scale results might have on the design a full-scale concept vehicle.

(a)

Figure 1. The NASA N3-X hybrid wing-body concept aircraft with turbo-electric distributed propulsion system.[3–5]

II. Experimental Setup and Data Acquisition

II.A. Test Facility

The High Flow Jet Exit Rig (HFJER) in the Aero-Acoustic Propulsion Laboratory (AAPL) at the NASA Glenn Research Center was used for these tests. The HFJER accepts single-stream, internally mixed, or separate flow nozzle systems providing flow temperatures up to 1200°F (925 K) on the core stream and

300°F (425 K) on the fan stream. Total mass flow rates up to 28 lbm/s (12.7 kg/s) can be achieved by combining the core and bypass streams. The HFJER sits inside the Nozzle Acoustic Test Rig (NATR), a 53-inch (1345 mm) diameter freejet tunnel capable of producing a simulated flight stream at speeds up to Mach 0.35. The AAPL is a geodesic dome (65-foot radius) lined with sound absorbing wedges to create a test environment that is anechoic for frequencies above 200 Hz. Details on the AAPL and HFJER can be found in [11-12]

II.B. Data Acquisition and Processing

Three distinct data sets were acquired during the test: far-field noise data, phased array noise source localization, and steady-state in-flow pressure. First, the far-field noise was measured using an array of 24 Bruel & Kjaer Type 4939 microphones. These microphones were mounted on an arc with a 45-foot radius centered on the nozzle exit and covered polar angles between $45° \leq \theta \leq 160°$ at 5° increments. Bruel & Kjaer Nexus units provided signal conditioning and amplification. A DataMAX Instrumentation Recorder from R.C. Electronics sampled the data at 200 kHz with a 90 kHz Nyquist filter. Once digitized, the time series data were converted to power spectral density (PSD) in the frequency domain using a standard fast Fourier transform routine with 2^{14} point Kaiser windows (50% overlap) giving a spectral resolution of 12.2 Hz. Next, the background noise, acquired before each test run, was subtracted on a power basis at each frequency $(PSD_T(f) \ominus PSD_B(f))$; if the background noise level was within 3 dB of the measured signal then the measured data at that frequency was removed from the spectrum. The PSD spectra were then corrected for the individual characteristics of each microphone using the calibration supplied by the manufacturer. Finally, the effects of atmospheric attenuation were removed and the data scaled to a distance of $100D_e$, where D_e is the diameter of a round nozzle with equivalent area. Non-dimensional Strouhal frequency scaling was applied using the nozzle equivalent diameter (D_e or the nozzle height (H_j), as appropriate, for the characteristic length.

Phased-array source localization data were acquired using an Array48 system from OptiNav, Inc. This system consists of 48 Earthworks M30 microphones flush-mounted to a 1 m × 1 m aluminum plate and arranged in a series of logarithmic spirals. The microphones have 1/4" (0.635 cm) diameter diaphragms and a flat frequency response over a frequency range of 5 Hz to 30 kHz. The array was placed at 90° to the jet plume and 2 m from the jet centerline such that the center of the array microphone plate was located axially at the nozzle exit plane. For each run, data were acquired for 45 seconds using the 24-bit, 96 kHz sample rate audio interface in Array 48 (MOTU 24I/O). Classical delay-and-sum beamforming was used to locate the dominant source within each of the processed $1/3^{rd}$-octave frequency bands. Phased-array data were collected for the isolated nozzles only.

In-flow total pressure data were acquired using a traversing probe downstream of the nozzle exit. Total pressure scans were run across the nozzle width (major axis) to estimate the initial jet profile and axially downstream from the nozzle exit to show the plume decay and estimate the jet potential core length.These data were also acquired only for configurations without the surface (isolated). The total pressure data were recorded using the AAPL facility ESCORT computer system. ESCORT simultaneously records the relevant temperatures and pressures that define the nozzle exit flow condition as well as the ambient atmospheric conditions used in the data processing and nondimensionalization. All data are sampled at 1 Hz and averaged over a 10 second period to report the steady state value.

The frequencies produced by high aspect-ratio jets are proportional to the nozzle height.

II.C. Test Hardware and Flow Conditions

Nozzle height is the key dimension when projecting noise data from a model-scale high aspect-ratio nozzle to a full-scale concept. The slot nozzle proposed for the N3-X concept (Figure 1) has an aspect-ratio of approximately 32:1 with an exit height that varies with the number of fans and the fan pressure ratio.[4] The HFJER, combining the core and fan streams, has a maximum flow rate of 28 lbm/s (11 kg/s); this flow rate defines the maximum nozzle exit area. A 32:1 aspect-ratio nozzle limited to the HFJER flow rate would have a nozzle height (H_j) of 1.1 in. (28.3 mm) and a nozzle width (W_j) of 35.64 in. (905.2 mm). These dimensions present two problems. First, the nozzle/plume is nearly as wide as the facility freejet making it unlikely that the jet plume would remain within the flight-stream (53 in./1345 mm at the exit plane and less downstream as the potential core closes out)[a]. Second, the scale-factor from this scale-model to the N3-X concept[b] is approximately 20; this scale-factor requires measuring model-scale frequencies up to 120 kHz to to project to full-scale while retaining the most weighted perceived noise level frequencies ($f \leq 6$kHz).This is above the capability of the data acquisition system and, therefore, the aspect-ratio was reduced for the model-scale test to 16:1. This aspect-ratio allows dimensions of $H_j = 1.57$ in. (40 mm) and $W_j = 25.2$ in. (640 mm) within the HFJER maximum flow rate and a scale-factor of 14.

A 16:1 aspect-ratio nozzle (A16M) was designed and manufactured specifically for this test. The design of this nozzle presented two particular challenges not present on the concept aircraft: the transition from a circular cross-section at the jet rig to a 16:1 aspect-ratio rectangle at the nozzle exit and the ability to accept variations in internal geometry (e.g. septa number, shape, location). First, transitioning from a round to rectangular cross-section introduces cross-flow and other flow nonuniformities, including a high probability for separated flow. The greater the aspect-ratio, the stronger these nonuniformities are. In contrast, each fan in the N3-X distributed propulsion system transition to a section of the exhaust nozzle with an aspect-ratio around 2:1. Thus, the scale-model must transition from a round to 16:1 aspect-ratio cross-section while providing a flat velocity profile at the nozzle exit, free from internal flow separations, across a wide range of Mach numbers, and without creating excess internal flow noise that might contaminate the jet noise measurements. Additionally, the axial length of the transition was restricted by the weight/moment limits of the HFJER; ensuring that the jet plume would remain within the flight stream was also a concern. Several design iterations were run using CFD to create the transition and nozzle; this process and resulting design is documented in reference [13].

The septa that separate the electric fans and divide the exhaust flow in the N3-X distributed propulsion concept were included in the nozzle design to add another element of realism to the model-scale test. A parametric study into how septa number, shape, and location effect the exhaust noise was planned and, therefore, the model-scale nozzle had to accept variations in the septa. A system was devised where a channel was cut near the nozzle exit and septa inserts could be slid in and out without damage[c]. These inserts were created using a 3D plastic printer making them relatively quick and inexpensive to design and build. However, unlike the N3-X, the septa in this design could not be structural members supporting the nozzle. A stress analysis showed that an unsupported nozzle with sufficient strength to prevent the pressure forces from changing the exit shape would be too heavy due to the material required (stainless steel) or amount of material (aluminum). Therefore, a single centervane, cut from 0.030" thick stainless steel, was added in the center of the nozzle to provide the additional strength needed to hold the nozzle shape. However, this solution required that the open nozzle/baseline have a single septum.

Parameters of the septa inserts tested are given in Table 1 and Figure 3 shows the septa inserts tested. Each septum was designed using a NACA 0003 profile with a 6-inch chord giving a maximum thickness of 0.18". A 0.025"-radius fillet was applied at the trailing edge to give it a rounded shape with sufficient thickness to withstand the flow forces; this shortened the overall length to approximately 5.4". Fillets (0.05"-radius) were also applied at the top and bottom of each septum to provide additional strength without increasing the overall thickness. The center septum was divided by the metal centervane with a half-airfoil on each side. Thus, the center septum had the same general shape as the other septa but with the extra thickness and blunt edge of the 0.03" thick metal centervane at the trailing edge. Finally, a linear contraction was added to the major-axis, terminating at the nozzle exit, to ensure continuous contraction through the septa to the nozzle exit; without this, the flow area would increase after the midpoint of the septa leading to concerns of flow separation or extraneous noise. As a result, the final nozzle exit height was $H_j = 1.34$" for all septa and the aspect-ratio was increased from the original design (see Table 3). Note that all nondimensionalizations will use $H_j = 1.34$" but the nozzle will be identified by its originally intended 16:1 design aspect-ratio for clarity.

Surfaces were attached flush with the nozzle exit to simulate the integrated aft-deck of the N3-X. Several surface lengths (x_E) were tested: 1.25", 3", 6", 9", and 12". Each surface was made from a single piece of 1/2" aluminum with a 45° bevel cut into the trailing edge. The surface span (y_E) was made wide enough so that flow would not reach the spanwise edges and the system could be considered as infinite in that direction. The nozzle/surface system was designed so that it could be mounted at different azimuthal angles (ϕ) relative to the fixed far-field microphone array. The rotations tested are shown in figure 4. Table 3 lists

---

[a] Although the flight stream was not used for this test due to complications with the surface/aft deck, it was planned for in a future entry.

[b] Based on data available in [3–5] for a 15-17 fans operating between $1.3 \leq FPR \leq 1.4$, $H_j \approx 22$" (559 mm).

[c] In practice the inserts were glued into the channel to seal any gaps after the first one was destroyed.

the configurations tested for far-field noise.

The jet flow conditions tested were selected to cover the operational range of the N3-X while respecting the limits of the test hardware. Table 2 shows the flow conditions (setpoints) tested. The approach condition, setpoint 3 ($M_a = 0.5$), is the lowest jet velocity that can be tested in the AAPL before the background noise begins to contaminate the measurements.[16,17] The high velocity condition, setpoint 7 ($M_a = 0.9$) is the representative takeoff condition; the nozzle was sized to require the (near) maximum flow rate of the HFJER at setpoint 7.

All jet flow conditions tested (Table 2) were unheated. The TeDP system uses a row of 15-17 electric fans operating in the $1.3 \leq FPR \leq 1.4$ range.[3–5] Each fan will increase the total temperature of the air passing through it but the increase will be relatively small. Additionally, heating the air stream has two practical implications on the test: (1) the nozzle must be capable of handling the extra heat without deforming adding weight and (2) test time is significantly increased due to the time needed to cool the nozzle before model changes. Therefore, the flow conditions were all unheated ($T_tR = 1$) for this test.

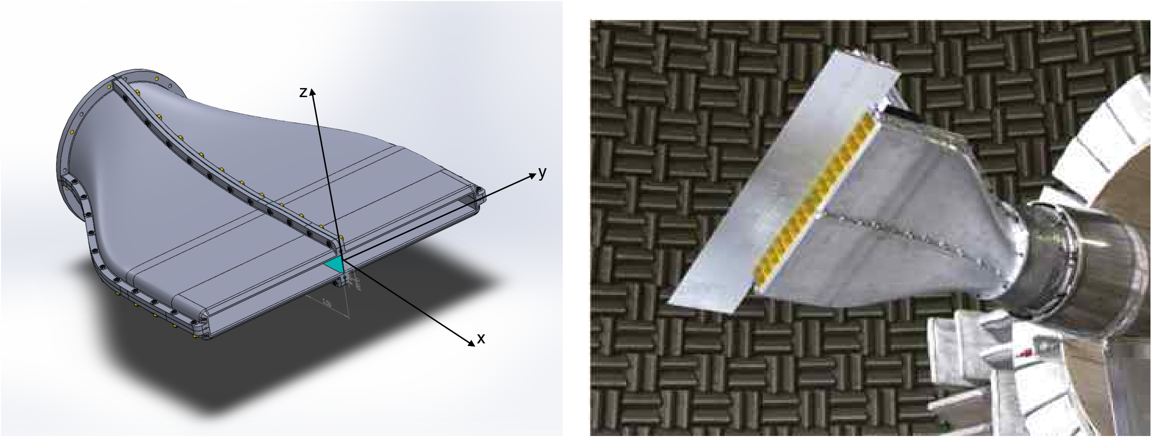

(a) 16:1 Nozzle

(b) 16:1 Nozzle with Septa and Surface

Figure 2. The 16:1 aspect-ratio rectangular nozzle, with coordinate system (left), and mounted to the HFJER with septa and aft-deck surface (right). Note that is only one row of septa; what may appear to be a second row is a reflection off the surface.

ID	A_j	Adj. Aspect-Ratio	Septa	Distributed Aspect-Ratio
I161	33.67	18.8	1	8:1
161A	33.34	18.7	7	2:1
161B	33.11	18.5	15	1:1

Table 1. Septa inserts tested. Note that total septa includes the fixed centervane. Adjusted (Adj.) aspect-ratio is defined using $H_j = 1.34$" and adjusting W_j to account for the thickness of the septa. Distributed aspect-ratio is defined by the area between septa. The inserts are shown in Figure 3.

Setpoint	$P_{t,j}/P_a$	M_a	T_tR
330	1.197	0.5	1
440	1.300	0.6	1
550	1.436	0.7	1
660	1.617	0.8	1
770	1.860	0.9	1

Table 2. Jet exit conditions tested with identifying setpoint numbers.

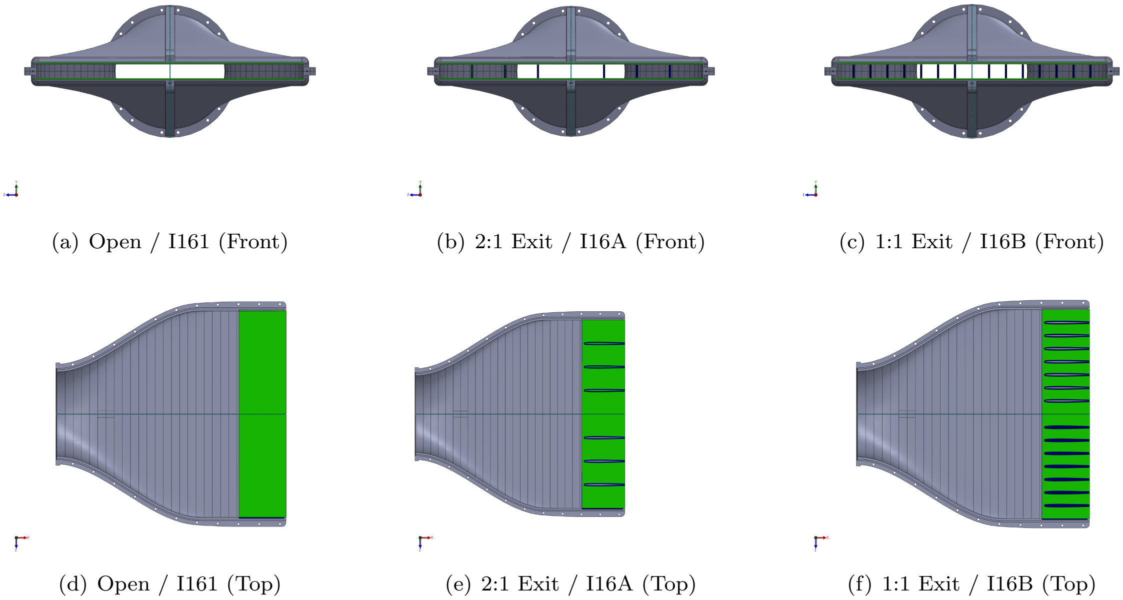
(a) Open / I161 (Front)　(b) 2:1 Exit / I16A (Front)　(c) 1:1 Exit / I16B (Front)

(d) Open / I161 (Top)　(e) 2:1 Exit / I16A (Top)　(f) 1:1 Exit / I16B (Top)

Figure 3. Nozzle and septa inserts tested. The septa (green) were printed in two parts; they are divided by the metal centervane when installed.

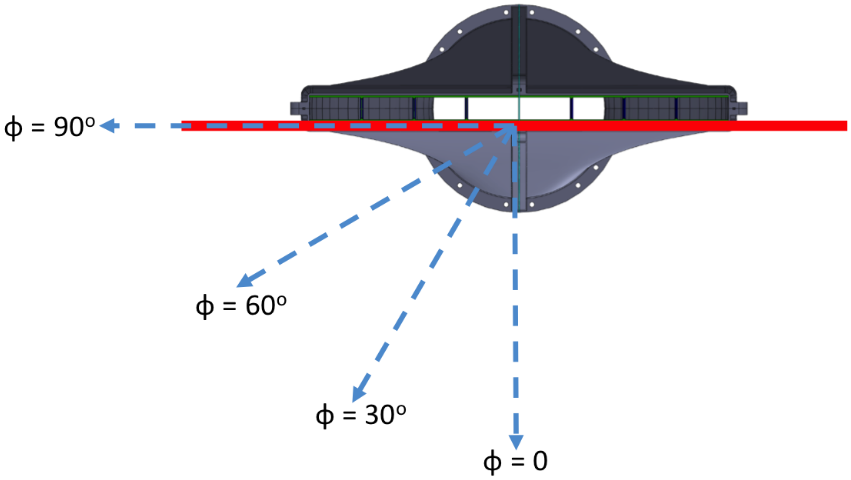

Figure 4. Azimuthal angles (ϕ), created using nozzle rotations to the fixed microphone array, where far-field noise data were acquired. The red line represents the surface location. Data were acquired on an arc (equal distance) but are shown extended to the ground plane (black line) for clarity.

Nozzle	Insert	xE (in)	$\phi = 0$	$\phi = 30$	$\phi = 60$	$\phi = 90$	$\phi = 180$
A16	I161	NA	x	x	x	x	
A16	I161	1.25	x	x	x	x	
A16	I161	3	x			x	
A16	I161	6	x	x	x	x	
A16	I161	9	x			x	
A16	I161	12	x	x	x	x	
A16	I16A	NA	x	x	x	x	
A16	I16A	1.25	x	x	x	x	
A16	I16A	3	x			x	
A16	I16A	6	x	x	x	x	
A16	I16A	9	x			x	
A16	I16A	12	x	x	x	x	
A16	I16B	NA	x			x	x
A16	I16B	1.25	x			x	x
A16	I16B	3	x			x	x
A16	I16B	6	x			x	x
A16	I16B	9	x			x	x
A16	I16B	12	x			x	x

Table 3. Configurations for the far-field noise portion of the test. Test nomenclature for the 16:1 aspect-ratio nozzle was "A16". The septa "I161", "I16A", and "I16B" are shown in Figure 3 and listed in Table 1.

III. Summary of Data Acquired

III.A. In-Flow Pressure Data

The total pressure in the flow near the nozzle exit was the first dataset acquired. These data served to validate the nozzle design by documenting an even flow profile across the nozzle width and without flow separations at the edges. A single rake with five pitot probes, aligned on the z-axis (Figure 2(a)), was mounted on a traverse to move across the length of the nozzle. The probe stopped every 0.25" to acquire data (after a short settling time). Figure 5(a) shows the probe near the nozzle exit. These results, shown in Figure 5(b)[d], confirm the nozzle design at the lowest (330) and highest (770) setpoints. Although there is some rounding at the edges due to the boundary layer at the nozzle wall, the pressure profile is generally flat across the nozzle at both setpoints. The exception is at the nozzle centerline where the centervane produces a significant deficit.

The next set of data were acquired by traversing the pressure probe downstream along the jet axis. There were two reasons for this: to estimate the strength and longevity of the deficit behind the centervane and to estimate the jet potential core length. Figure 6(a) shows the results from an axial traverse behind the centervane ($y = 0$, $z = 0$) at setpoints 330, 550, and 770. The total pressure is below the setpoint (Table 2) near the nozzle exit in each case and the reduction is greatest at setpoint 770; these observations are consistent with the data in Figure 5(b). The pressure increases as the flow moves downstream and the centervane wake dissipates but the full setpoint pressure pressure is never recovered (i.e. the wake deficit persists past the end of the jet potential core).

The jet potential core length (x_C) has been used as a normalizing parameter in jet velocity,[14,15] noise source distribution,[8] and JSI noise models.[20,22] Figure 6(b) shows the total pressure measured along an axial traverse at $z = 0$, $y = 6.25$", the midpoint between the centervane and the lengthwise edge. The total pressure at this location matches the setpoint pressure near the nozzle exit, again consistent with Figure 5(b). However, without the centervane wake, the flow holds the setpoint total pressure until the approximate end of the jet potential core. These data can, therefore, be used to estimate the potential core length. The

---

[d] Authors' Note: In order to maximize the data available in this document, the data plots have been produced in vector-based PDF format to allow on-screen enlargement without loss of quality.

method, outlined for velocity data by Bridges in [14], uses a linear fit in logarithmic space to find the decay rate. The potential core length is then defined as the point that the decay rate line intersects the setpoint value. The starting point for this method is the equation:

$$\phi = 1 - exp\left\{ \frac{\alpha}{1-\frac{X}{\beta}} \right\} \tag{1}$$

where ϕ is the normalized source data (i.e. pressure or velocity), α is the decay rate, β is the nondimensional potential core length and X is the axial distance nondimensionalized by the nozzle length-scale. Note that for the nozzle length-scale high-aspect ratio nozzle is the height (H_j) so that $\beta = x_C/H_j$ and $X = x/H_j$. In this case, ϕ is the nondimensionalized total pressure given as:

$$\phi = \frac{P_{t,j}(x) - P_a}{P_{t,j}(x=0) - P_a} \tag{2}$$

where $P_{t,j}(x=0)$ is the total pressure set at the jet exit plane, $P_{t,j}(x)$ is the total pressure measured in the jet plume, and P_a is the ambient pressure. Equation 1 can be solved for α as:

$$\alpha = \left[1 - \frac{X}{\beta}\right] ln(1-\phi) \tag{3}$$

and rearranged to:

$$X ln(1-\phi) = \beta ln(1-\phi) - \alpha\beta \tag{4}$$

A linear fit to the points $(Xln(1-\phi), \beta ln(1-phi) - \alpha\beta)$ will have slope β and intercept $-\alpha\beta$. The resulting values for setpoints 330, 550 and 770 are shown in Table 4. Note that the decay rate (α) will be different when total pressure is used in place of velocity but β will be the same.

Setpoint	α	β	β_{SSS}
330	1.997	4.64	4.38
550	1.915	4.83	5.04
770	1.742	5.66	5.77

Table 4. Pressure decay rate (α) and potential core length (β). The value of β predicted using the Simple Single Stream (β_{SSS}) model,[14,15] developed using velocity data from round jets, is included for comparison.

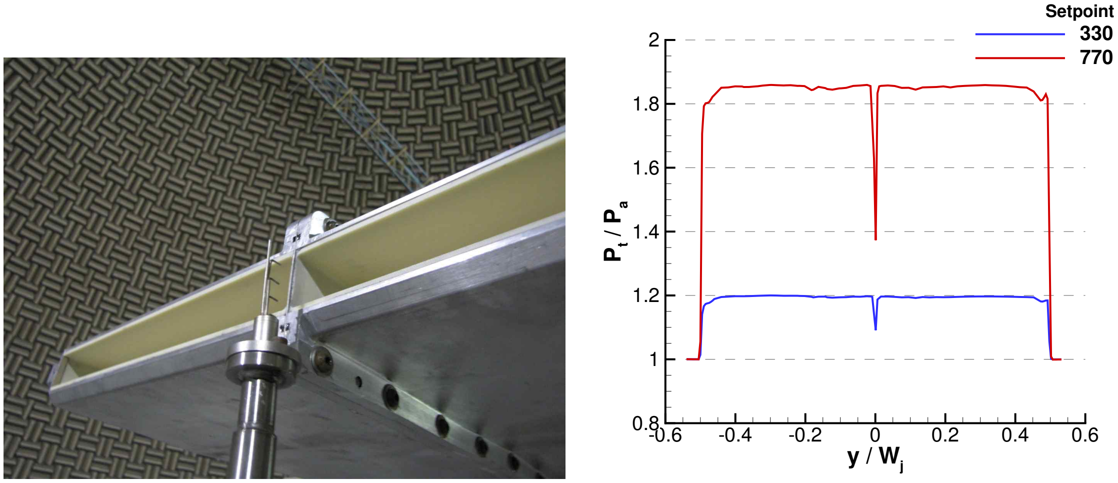

(a) Pressure Probe

(b) P_t/P_a at $x = 0.25$”, $z = 0$

Figure 5. Total pressure probe mounted in front of the nozzle (left) and total pressure measured at $x = 0.25$”, $z = 0$ for setpoints 330 and 770 using the I161 septa (right).

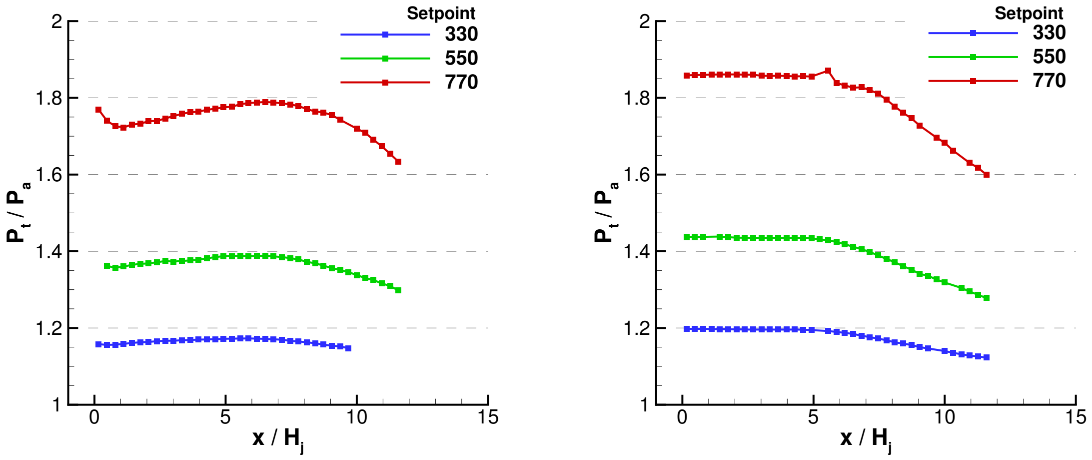

(a) $y = 0$, $z = 0$ (b) $y = 6.25$", $z = 0$

Figure 6. Total pressure in the jet flow, relative to ambient pressure, measured using the I161 septa traversing downstream at $z = 0$ behind the centervane ($y = 0$) and at $y = 6.25$".

III.B. Phased-Array Source Localization Data

Phased array source location data were acquired using the isolated (no surface) configurations with the I161 and I16A septa inserts with two goals: document the distribution of the jet-mixing noise sources to develop/improve noise shielding models and investigate the effect of septa on the source distribution. Figure 7 shows the axial location of the peak source in the phased array map as a function of frequency. These peak axial locations were extracted from 2-dimensional phased-array source maps in the x-y plane (e.g. Figure 8); the imaged plane is important because the phased-array source maps may change depending on the azimuthal angle imaged. The resulting source distribution follows the generally expected behavior of jet-mixing noise sources, moving closer to the nozzle exit as frequency increases,[8] until the peak source location jumps to the nozzle exit. The frequency where this jump occurs is dependent on jet velocity and septa design.

The noise source localization maps for setpoint 330 with the I161 and I16A septa designs at 1/3-octave frequencies between 4 kHz and 10 kHz are shown in Figure 8. These maps provide insight into the discontinuous source location behavior observed in Figure 7. The I161 septa design (Figure 8, left column) produces sources at $f = 4$ kHz and $f = 5$ kHz that are downstream of the nozzle exit in the plume indicating that the jet-mixing noise is dominant. The jet-mixing source remains dominant at $f = 6.3$ kHz (Figure 8(f)) but the first indication of a new source appears at the trailing edge of the centervane. This second source then becomes dominant at $f = 8$ kHz (Figure 8(g)), the frequency corresponding to the sudden change of peak source location observed in Figure 7; the mixing noise source is still present in the jet plume at this frequency. Finally, at $f = 10$ kHz, all of the dominant sources appear at the nozzle exit. A similar pattern emerges with the I16A septa design (Figure 8, right column): the jet-mixing noise source is dominant at low frequencies ($f = 4$ kHz, Figure 8(b)), there is a sudden change of peak source location when the dominant source goes to the trailing edge of the septa ($f = 5$ kHz, Figure 8(d)) while the jet-mixing noise sources steadily move closer to the nozzle exit at higher frequencies ($f = 10$ kHz, Figure 8(j)).

The peak jet-mixing noise source locations from a single-stream round jet, nondimensionalized by the jet potential core length, trends logarithmically to the nozzle exit as the source Strouhal frequency increases.[8] A similar trend can be found for the 16:1 aspect-ratio rectangular nozzle with the I161 septa using the jet potential core lengths determined in Section III.A and the peak noise source locations (Figure 7(a)). First, jet-mixing noise source locations (i.e. those before the source location jumps to the nozzle exit) are nondimensionalized by the jet-potential core length and the corresponding frequencies are converted into Strouhal frequencies; in both cases the nozzle height (H_j) is used for the critical length-scale. Then a linear trend line, in logarithmic frequency, is fit to these data to find:

$$\frac{x}{x_C} = \frac{x}{\beta H_j} = -2.074\, log_{10}(St_{Hj}) + 1.06 \tag{5}$$

In-flow pressure data were not acquired along the jet axis using the I16A septa design so a similar trendline can not be fit directly to these source data (β is not known). Figure 9(b) was created assuming that β is the same for the two septa designs and, therefore, the peak jet-mixing noise source locations will collapse to the same trend line. However, the peak noise sources are upstream of the trend line across the frequency range. The phased-array source location data has shown throughout this analysis that the I16A septa design (1) moves the peak jet-mixing noise sources slightly upstream relative to the more open I161 design and (2) the peak noise source jumps to the nozzle exit at a lower frequency than the I161 septa. One hypothesis for this behavior is that the septa promote mixing in the jet plume by generating trailing edge vortices and, therefore, shorten the potential core. Assuming this is the case and that this relationship is linear, it is possible to estimate the potential core length for the I16A septa design using the difference in source locations such that:

$$\beta_{I61A} = \frac{x_{I16A}(f)}{x_{I161}(f)}\beta_{I161} \qquad (6)$$

where $x(f)$ is the source location at each frequency and the subscripts $I16A$ and $I16I$ represent the different septa designs. Note that Equation 6 will give a slightly different value for β_{I16A} at each frequency due to uncertainties in the data and fitting process so the values of $\beta_{I16A}(f)$ are averaged to get a single result at each setpoint: $\beta_{I16A} = 4.42$ at setpoint 330, $\beta_{I16A} = 4.56$ at setpoint 550, $\beta_{I16A} = 5.07$ at setpoint 770. The source locations for the I16A septa, now nondimensionalized by β_{I16A}, are shown in Figure 10; compared to Figure 9(b) where β_{I161} was used, the agreement with the previously established trend line (Equation 5 is significantly improved. Thus, this use of the peak source distribution appears to give a reasonable estimate of the potential core length in a rectangular jet with septa[e]. This analysis also supports the hypothesis that the septa shorten the potential core which may have implications for shielding jet-mixing noise sources by airframe surfaces.a

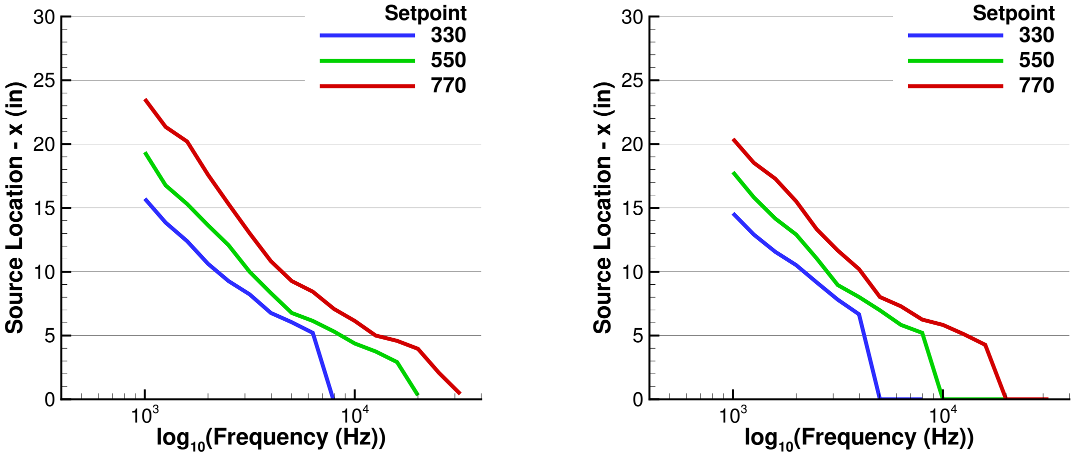

(a) I161

(b) I16A

Figure 7. Peak noise source locations determined by phased array analysis with the I161 (left) and I16A (right) septa inserts.

---

[e] Total pressure data were not acquired on the jet axis with the I16A septa design due to the limited test time available. Therefore, a direct comparison of β is not available.

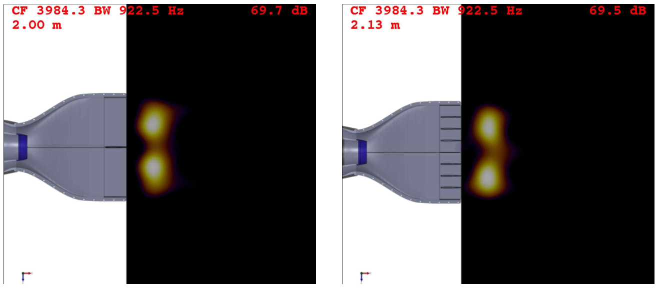

(a) I161, $f = 4$ kHz (b) I16A, $f = 4$ kHz

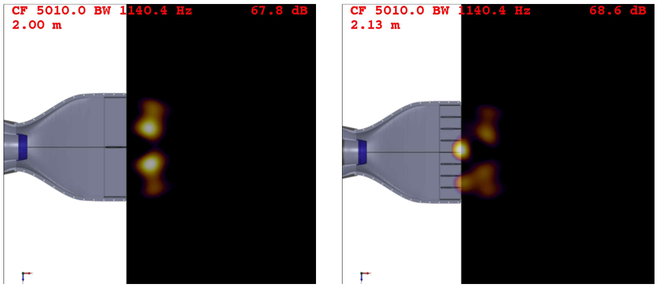

(c) I161, $f = 5$ kHz (d) I16A, $f = 5$ kHz

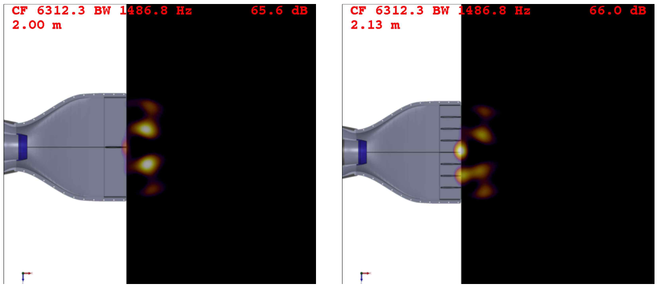

(e) I161, $f = 6.3$ kHz (f) I16A, $f = 6.3$ kHz

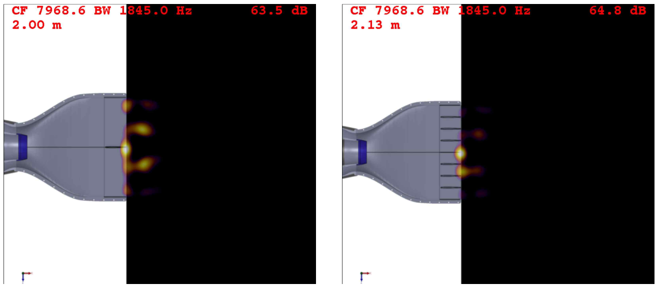

(g) I161, $f = 7.9$ kHz (h) I16A, $f = 7.9$ kHz

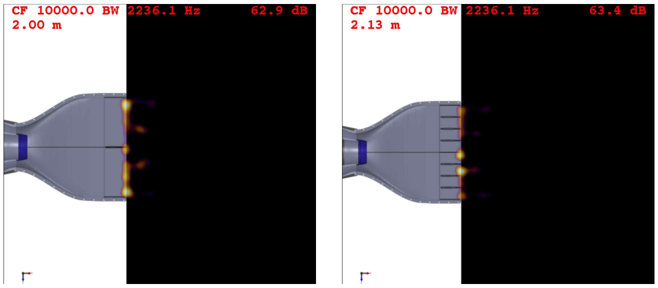

(i) I16I, $f = 10$ kHz (j) I16A, $f = 10$ kHz

Figure 8. Noise source location maps imaged by the phased array at setpoint 330 using septa inserts I161 (left) and I16A (right)

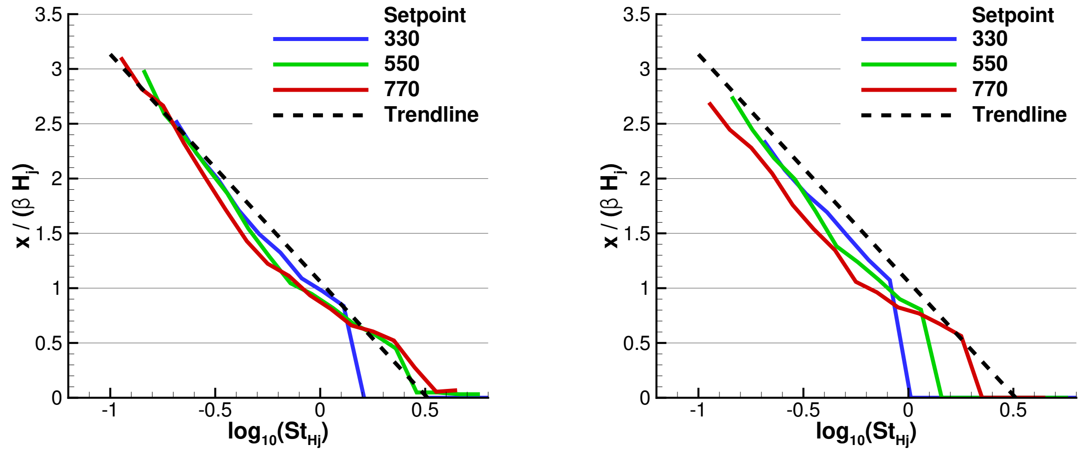

(a) I161

(b) I16A

Figure 9. Noise source locations determined by phased array analysis nondimensionalized by potential core length (β) and nozzle height (H_j) with Strouhal frequency scaling.

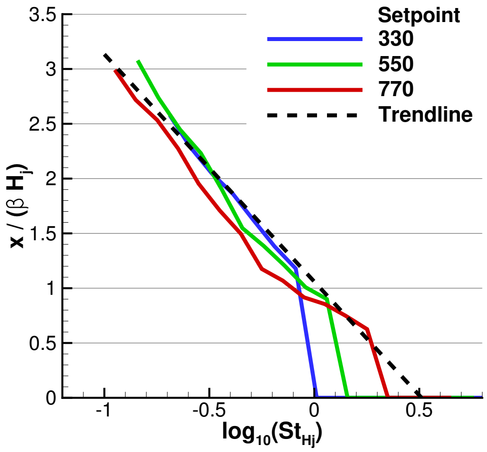

Figure 10. Noise source locations determined by phased array analysis for the A16A septa design nondimensionalized by the potential core length (β) estimated by Equation 6 and nozzle height (H_j) with Strouhal frequency scaling.

III.C. Far-Field Noise Data

III.C.1. Isolated Jet Noise

There are three important pieces to consider in the exhaust of the N3-X concept (Figure 1): (1) the high-aspect ratio nozzle exit, (2) the septa that divide the fan flow into channels, and (3) the aft-deck. First, Figure 11 shows the effect of increasing nozzle aspect-ratio in isolation (i.e. no surface) by using data acquired in previous tests[10, 21, 22] for comparison. The general trend at low frequencies is an immediate noise increase from the round shape to the lowest aspect-ratio rectangular nozzle (2:1) followed by smaller changes as aspect ratio increases from 2:1 to 16:1; in fact, the is very little difference between the 8:1 and the 16:1. The opposite trend occurs at high frequencies; excluding the 16:1 aspect ratio nozzle, each decrease in aspect ratio produces more noise up to the round nozzle. The 16:1 aspect ratio nozzle, however, produces more high frequency noise than the round nozzle, opposing the trend established by the lower aspect ratio nozzles (this behavior is most obvious in Figures 11(b) and 11(c) but is present to some extent at all setpoints and observer angles). This inconsistency at the highest aspect ratio has a few potential causes: for example, an internal noise source produced in the round-to-rectangular transition or a flow disturbance introduced by the centervane. A source internal to the nozzle might appear to be located at the nozzle exit and, depending on the size of the source region, could be in the higher frequency range. Alternatively, the centervane could cause a flow disturbance, such as vortex shedding from the trailing edge, that would cause a tone directed towards the major-axis ($\phi = 90°$) and could amplify the jet-mixing noise directed towards $\phi = 0$. There is some evidence for tones (e.g. screech or resonance tones[23]) amplifying broadband sources although it can not be confirmed that this is the case here.

Classic vortex shedding tones occur at $St_l = 0.2$ where l is the cross-stream length of the object. Thus, if the tone frequency and flow velocity are known then the cross-stream length-scale of the source object can be identified. Figure 12 shows the far-field noise spectra measured at $\phi = 90°$, $\theta = 90°$ using the I161 and I16A septa designs. The I16A septa produce a strong shedding tone that tracks to higher frequencies as the flow velocity increases (Figure 12(b)). These tones correspond to a cross-stream length scale of approximately $l = 0.05$ in., the nominal thickness of the airfoil septa near the trailing edge; similar tones have been observed in previous experiments.[24] The I161 insert, however, has only the centervane septum and produces tones only at the lowest velocity setpoints (Figure 12(a)); these tones correspond to a cross-stream length scale of approximately $l = 0.105$ in. The centervane was 0.03" thick and the septa insert, with a half-airfoil on each side of the centervane, added approximately 0.05" to create an approximate trailing-edge thickness of 0.08". There are a few possible explanations for this behavior. One hypothesis is that there is a separation somewhere in the nozzle at the lower velocity setpoints that goes away as the pressure and mass flow rate increase. In this scenario the tone does not appear in spectra produced by the I16A septa design because the additional septa back-pressure the nozzle disrupting the separation. The problem with this hypothesis is that the noise spectra produced by flow separations tend to be more broadband ('haystack') than pure tonal unless there is some particular geometric feedback loop. A second hypothesis is that these tones are produced by vortex shedding off the centervane but that the length scale is slightly longer either because (1) the flow separates from the half-airfoil on either side before the trailing edge or (2) the boundary layer thickness built up on the centervane through the round-to-rectangular transition gives the trailing edge the appearance of a slight longer cross-stream length. This hypothesis is supported by the azimuthal directivity of the tonal peak; as shown in Figure 13(b), the tone peaks at $\phi = 90°$ and disappears at $\phi = 0$ following the expected directivity of a JSI source at the trailing edge of the centervane. Phased-array data acquired at $\phi = 90°$ were processed using several planes on the nozzle major-axis in an attempt to determine if the source was located on the centervane but these efforts were inconclusive. Nevertheless, the most likely hypothesis is that these tones are related to an interaction between the flow and the centervane.

Far-field noise data were acquired using the I161 and I16A septa at azimuthal angles $\phi = 0, 30°, 60°, 90°$ to investigate the noise produced at the flyover and sideline points. The I161 septa design was selected as the baseline for this study, as the most similar to an open nozzle, and the I16A design was selected for comparison, as the most similar to the N3-X concept. Figures 13 and 14 show the spectral variations with azimuthal angle at setpoints 330, 550, and 770 for the I161 and I16A septa designs respectively. The general trend that emerges from these plots is an increase in the peak amplitude and a decrease in high frequency noise as azimuthal angle increases. Additionally, the Strouhal shedding tone from the vanes emerges as the azimuthal angle moves toward $\phi = 90°$, consistent with the expected directivity of these tones. Finally, the spectra are grouped so that majority of the change occurs between $\phi = 30°$ and $\phi = 60°$ (Figure

14). This has significant implications for predicting the sideline noise for the concept aircraft; if a takeoff profile, for example, is assumed then interpolation will be required to estimate the noise at azimuthal angles $30^\circ \leq \phi \leq 60^\circ$.

The final set of data acquired considered the effect of adding septa to the nozzle. The I16B septa were designed to present a series of 1:1 aspect ratio rectangles at the nozzle exit by doubling the number of septa in the I16A design; the septa themselves were otherwise identical. Figure 15 compares the far-field noise spectra of the I16A and I16B septa at azimuthal observer angles $\phi = 0$ and $\phi = 90^\circ$ [f]. Note that these data have been adjusted for the slight decrease in nozzle exit area caused by the additional septa (using $\Delta PSD = 10\,log_{10}(A_1/A_2)$). The results show that the effect of the septa number is relatively small on the overall noise levels throughout most of the frequency range. The most significant difference is that the Strouhal shedding tone is stronger when there are more septa, affecting the tone amplitude and nearby frequencies. In fact doubling the number of septa doubles the tone amplitude (6 dB, Figure 15(d)). Several other variations on septa design were considered but were not built or tested due to time limitations in the test facility; many of these have since been investigated on a smaller-scale.[24]

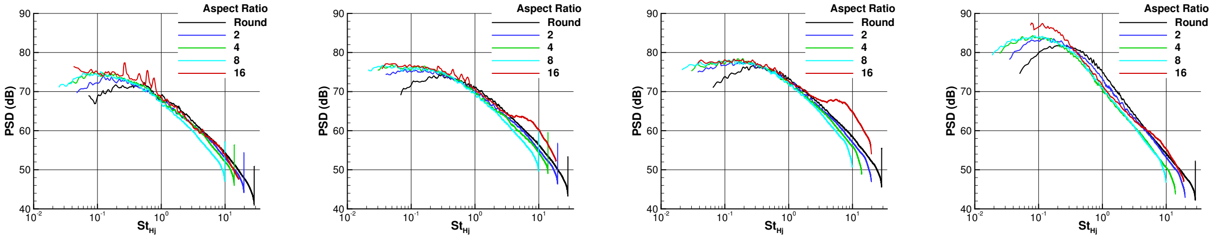

(a) SP 330, $\theta = 60^\circ$ (b) SP 330, $\theta = 90^\circ$ (c) SP 330, $\theta = 120^\circ$ (d) SP 330, $\theta = 150^\circ$

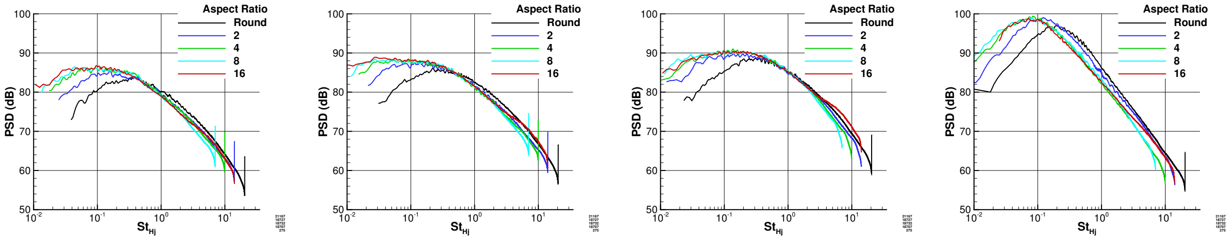

(e) SP 550, $\theta = 60^\circ$ (f) SP 550, $\theta = 90^\circ$ (g) SP 550, $\theta = 120^\circ$ (h) SP 550, $\theta = 150^\circ$

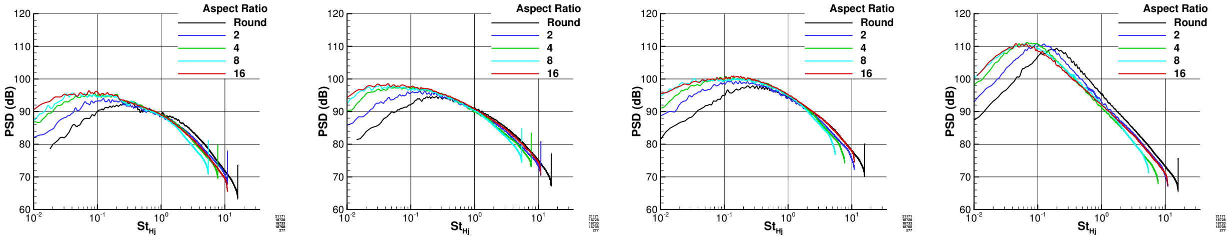

(i) SP 770, $\theta = 60^\circ$ (j) SP 770, $\theta = 90^\circ$ (k) SP 770, $\theta = 120^\circ$ (l) SP 770, $\theta = 150^\circ$

Figure 11. Effect of nozzle aspect ratio on far-field noise measured at observer angles $\phi = 0$, $\theta = 60^\circ, 90^\circ, 120^\circ, 150^\circ$ for setpoints (SP) 330, 550, and 770. Note the different spectral fall off at the highest frequencies is caused by the Nyquist filter on the data acquisition system rather than any physical phenomenon.

---

[f] Authors' Note: The scale is adjusted when presenting these 3-dimensional contour plots to better show the spectral shape; choosing the minimum and maximum from all data in a set (e.g. 40 to 110 PSD (dB) in Figure 15) tends to flatten the spectra shape. Please take note of the scale when viewing these plots.

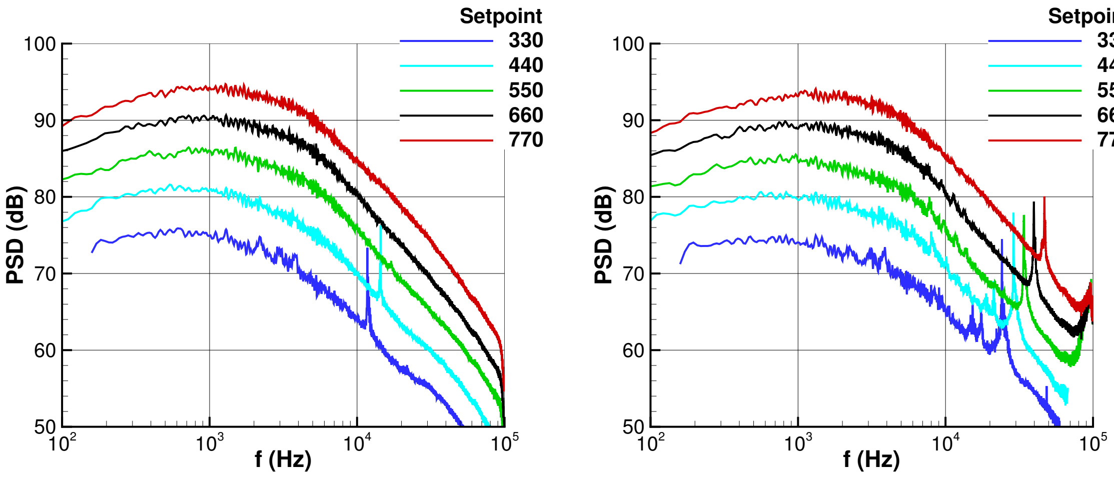

(a) I161 (b) I16A

Figure 12. Far-field noise measured at $\phi = 90^\circ$ and processed to a one-foot lossless condition.

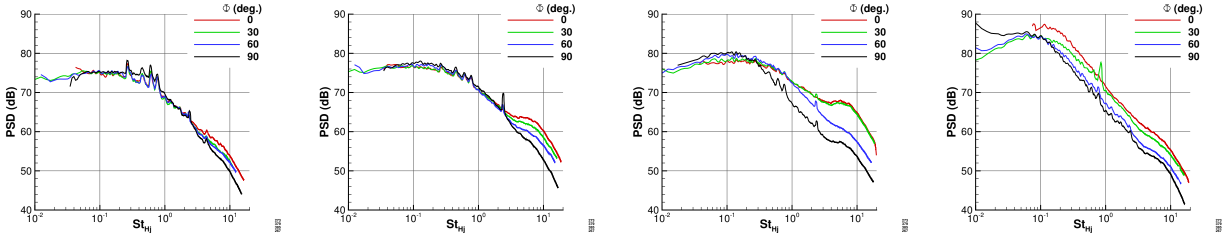

(a) SP 330, $\theta = 60^\circ$ (b) SP 330, $\theta = 90^\circ$ (c) SP 330, $\theta = 120^\circ$ (d) SP 330, $\theta = 150^\circ$

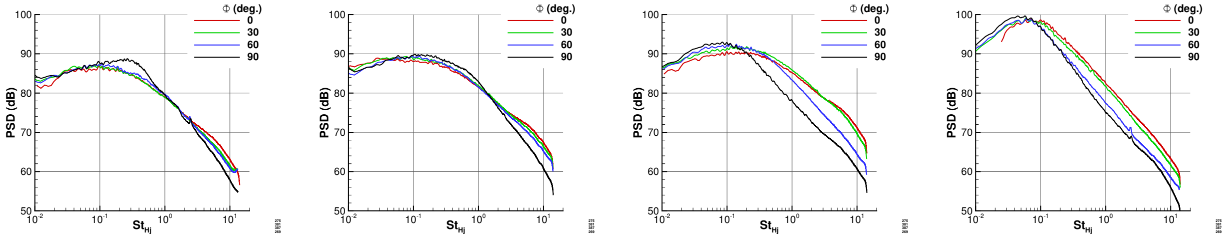

(e) SP 550, $\theta = 60^\circ$ (f) SP 550, $\theta = 90^\circ$ (g) SP 550, $\theta = 120^\circ$ (h) SP 550, $\theta = 150^\circ$

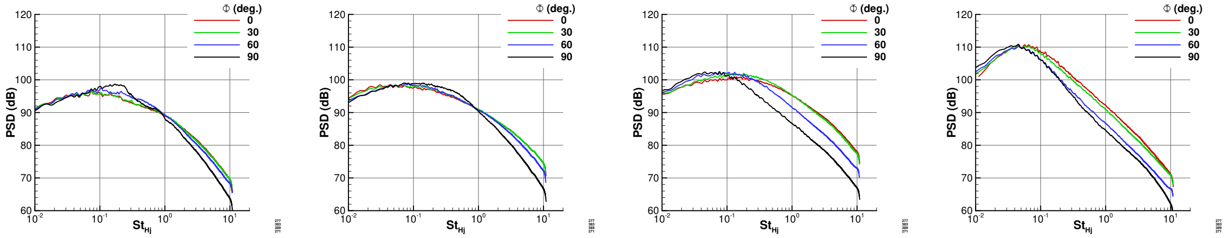

(i) SP 770, $\theta = 60^\circ$ (j) SP 770, $\theta = 90^\circ$ (k) SP 770, $\theta = 120^\circ$ (l) SP 770, $\theta = 150^\circ$

Figure 13. Spectra observed at polar angles $\theta = 60^\circ, 90^\circ, 120^\circ, 150^\circ$ and azimuthal $\phi = 0, 30^\circ, 60^\circ, 90^\circ$ for septa I161 at setpoints (SP) 330, 550, and 770.

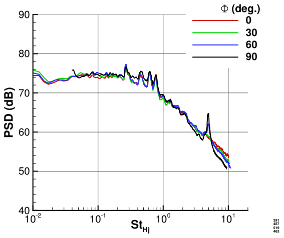

(a) SP 330, $\theta = 60^\circ$ (b) SP 330, $\theta = 90^\circ$ (c) SP 330, $\theta = 120^\circ$ (d) SP 330, $\theta = 150^\circ$

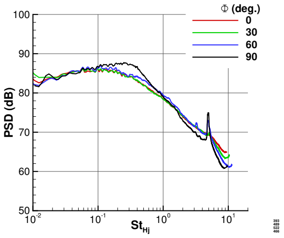

(e) SP 550, $\theta = 60^\circ$ (f) SP 550, $\theta = 90^\circ$ (g) SP 550, $\theta = 120^\circ$ (h) SP 550, $\theta = 150^\circ$

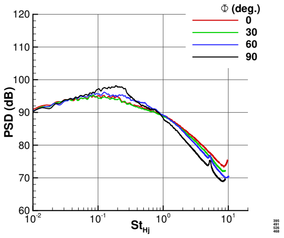

(i) SP 770, $\theta = 60^\circ$ (j) SP 770, $\theta = 90^\circ$ (k) SP 770, $\theta = 120^\circ$ (l) SP 770, $\theta = 150^\circ$

Figure 14. Spectra observed at polar angles $\theta = 60^\circ, 90^\circ, 120^\circ, 150^\circ$ and azimuthal angles $\phi = 0, 30^\circ, 60^\circ, 90^\circ$ for septa I16A at setpoints (SP) 330, 550, and 770.

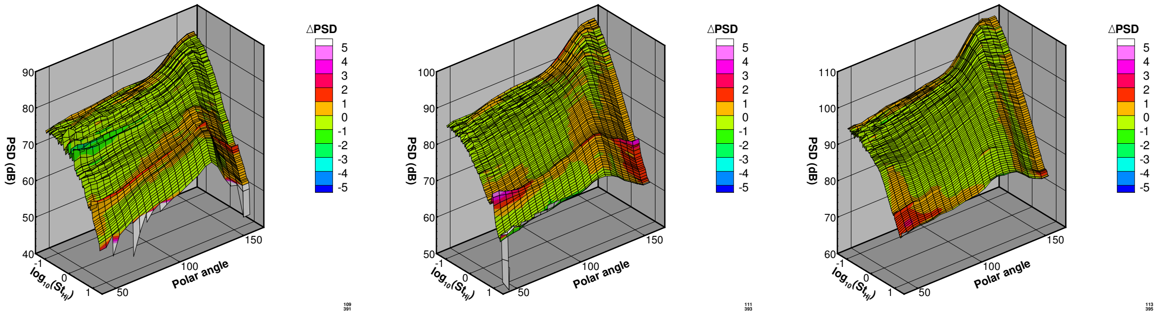

(a) SP 330, $\phi = 0$ (b) SP 550, $\phi = 0$ (c) SP 770, $\phi = 0$

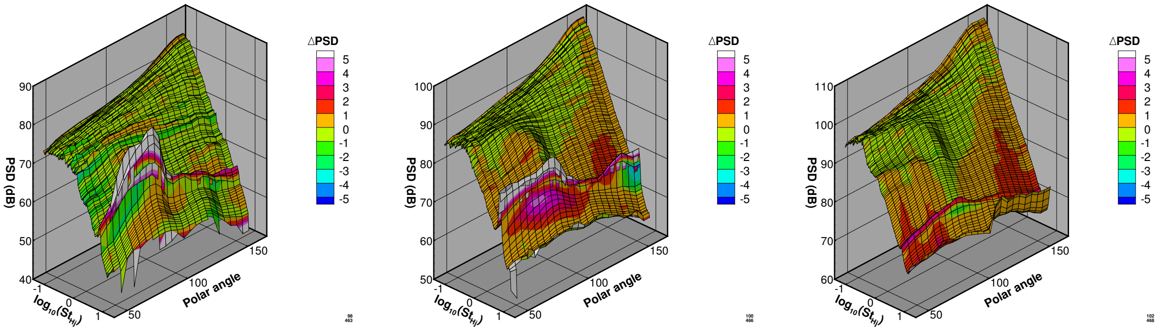

(d) SP 330, $\phi = 90°$ (e) SP 550, $\phi = 90°$ (f) SP 770, $\phi = 90°$

Figure 15. Spectral comparison between the I16A and I16B septa designs at setpoints (SP) 330, 550, and 770 where the spectra shape is from the I16B and the color contour is $\Delta PSD = PSD_{I16B} - PSD_{I16A}$. Note the change in scale on the z-axis (PSD (dB)) between the plots.

III.C.2. Installed Exhaust System Noise

The two propulsion components of the N3-X concept under consideration during this test are the high aspect-ratio nozzle, with septa, and the noise impact of the aft deck. The noise produced by the nozzle in isolation, presented in Section III.C.1, will serve as baseline for the noise produced or shielded by the aft deck. Figure 16 compares the noise at setpoint 330 with the three different inserts and the $x_E = 1.25$” surface to the noise produced without the surface (i.e. the spectral shape is with the surface and color contour is $\Delta PSD = PSD_{surface} - PSD_{isolated}$). The isolated jet at this setpoint created more high frequency noise at broadside angles than expected based on a trend analysis of aspect ratio (Figure 11). The shortest surface reduces most of that increased high frequency noise for broadside observers at $\phi = 0$ between $80 \leq \theta \leq 120$ but not at angles farther downstream. Otherwise, a surface with length on the order of the nozzle exit height ($x_E = 1.25$” to $H_j = 1.34$”) does not appear to have a significant effect.

The spectra measured with the I161, I16A, and, except for a stronger Strouhal shedding tone, I16B septa are remarkably similar (Figure 16). Therefore, the analysis in this section will focus on the data acquired with the I16A septa: (1) the I16A did not exhibit the unexplained tone at $\phi = 90°$ produced by the I161 septa (Figure 12) but (2) the results are otherwise similar, and (3) the I161A septa design produces a weaker Strouhal shedding tone than the I16B septa design (Figure 15). The I16A septa are also the closest in design to the N3-X concept that was the original motivation for this test and, therefore, will be used in Section IV.

Figure 17 shows the spectral variations with surface length and jet exit velocity (setpoint) relative to the isolated jet-mixing noise using the I16A septa design. The surface has the most effect on the noise measured when the jet velocity is lowest (setpoint 330) for two reasons: (1) the isolated noise at setpoint 330 showed an increase at high frequencies and broadside angles that decreased as velocity increased (Figure 11) and (2) the noise source distribution tracks with potential core length and, therefore, moves farther from the nozzle exit as velocity increases (Section III.B). The first point was discussed previously. The second point demonstrates the interplay between source location, set by the jet exit conditions, and surface length; the surface length can be increased for more noise reduction via shielding or the source distribution can be moved closer to the nozzle exit by reducing the jet exit velocity or, perhaps, though some mixing enhancement device (e.g.

chevron nozzles or septa). Thus, Figure 17 shows a decrease in shielding as setpoint increases from 330 to 770 (where the shielding effect is minimal).

While the lower velocity jet conditions benefit from increasing shielding at high frequencies, they are also penalized by an increase in low frequency noise created by the jet-surface interaction (JSI). The JSI noise in these cases is dominated by the trailing edge ('scattering') source, a dipole source located near the trailing edge of the surface that scales a U_j^6. Since the jet-mixing noise scales as U_j^8, the trailing edge noise is present, and indeed higher amplitude, at the higher velocity setpoints but is gradually overcome by the jet-mixing noise to produce a spectral and directivity shape more closely resembling the jet-mixing noise alone. However, this JSI source adds more than 10 dB to the low frequency noise at setpoint 330 ($x_E \geq 6$), 5-10 dB at setpoint 550 ($x_E \geq 6$), and 4-5 dB at setpoint 770 ($x_E = 9$"). The dipolar directivity of the JSI source and the aft dominate directivity of the jet-mixing noise result in these noise increases primarily at upstream and broadside observer angles (generally $\theta \leq 130°$) closer the minor-axis of the nozzle ($\phi = 0$). The surface, therefore, must be optimized with the jet exit conditions for maximum benefit while minimizing the penalty; simply adding more surface length may create more noise than it shields. (Note that scale factor is a critical part of this optimization and will be discussed in Section IV.)

The final point on the plots in Figure 17 is the tone in Figures 17(k) and 17(o) that extends across most polar angles. These combinations of jet velocity and surface length create a sort of resonance between the flow and the plate to produce this tone. They can, particularly at setpoint 770, send the surface into a regular low frequency vibration. While there has been some work done at smaller-scale to understand the source of these interactions,[18] these conditions were generally avoided during this test so as not to damage the test hardware.

III.C.3. Noise Source and Effect Noise Separation

The jet-surface spectra in Figure 17 are a combination of (at least) three different components: the jet-mixing noise, the JSI trailing edge noise, and surface shielding effect (i.e. the surface blocking the jet-mixing noise from the observer). The first two components represent noise sources while the third is an effect that modifies a source. Using these definitions and following the methodology similar to Reference [25][g], the measured (or total) power spectral density (PSD_T) can be constructed as:

$$PSD_T = (PSD_M + G_S) \oplus PSD_D \tag{7}$$

where PSD_M is the independently measured jet-mixing noise source (Section III.C.1), PSD_D is the dipolar JSI trailing edge noise source, and G_S is the surface effect on the jet-mixing noise and $\oplus$ indicates addition on a power (anti-logarithmic) basis. Equation 7 contains two unknowns so another equation is required to solve for G_S and PSD_D. However, because PSD_D is a dipolar source, it will be coherent over a range of observer angles where the distributed source jet-mixing noise is incoherent assuming that PSD_D is a compact source at the surface trailing edge. This assumption is not strictly true as the flow, and therefore the source, is distributed over some length of trailing edge depending on the nozzle aspect-ratio, jet-spread rate, and surface length; the incoherent portion PSD_D will be allocated to the surface effect G_S. Thus, the relative coherence can be used under this assumption to separate PSD_D from PSD_T by:

$$PSD_D = \gamma_{\theta 1,\theta 2} PSD_T \tag{8}$$

where $\gamma_{\theta 1,\theta 2}$ is the coherence between two observers centered at θ and separated by $\Delta\theta = 40°$; this is the minimum range over which the jet-mixing noise was incoherent. Note that the maximum dynamic range with this technique is approximately 12-14 dB. Now the surface effect can be found by solving Equations 7 and 8 to find:

$$G_S = (PSD_T \ominus PSD_D) - PSD_M \tag{9}$$

where $\ominus$ indicates subtraction on a power (anti-logarithmic) basis. This method allows comparisons between the different sources and effects as jet velocity and surface length varies.

---

[g] Reference [25] used the coherence around $\theta = 90°$ to extract PSD_D. The method used here differs only by using the coherence around each angle, e.g. $PSD_D(\theta = 60) = \gamma(\theta 1 = 45, \theta 2 = 85) PSD_T(\theta = 60)$, $PSD_D(\theta = 90) = \gamma(\theta 1 = 70, \theta 2 = 110) PSD_T(\theta = 90)$, etc. The size of the range, ±20°, was selected as the minimum range over which the isolated jet noise was incoherent.

III.C.4. JSI Noise Source (PSD_D)

Equation 8 allows investigation of the trailing edge source separately from the other effects. First, consider the effect of nozzle aspect ratio on PSD_D. Figure 18 shows PSD_D for the $x_E = 3$" and $x_E = 6$" surfaces with the 16:1 nozzle at setpoint 330 compared with PSD_D from an 8:1 aspect ratio nozzle near a similar simple surface but at smaller scale.[10] These data were selected using nondimensionalized surface length, x_E/H_j, to account for variations in nozzle aspect ratio and scale-factor. This nondimensionalization is also approximately equivalent using jet potential core length, or $x_E/(\beta * H_j)$ which has been used effectively in empirical JSI noise models to describe the flow at the surface trailing edge.[22] In this case, nondimensionalizing by H_j leaves nozzle aspect ratio as the primary varying parameter in these spectra. The PSD_D spectra from the 16:1 aspect ratio nozzle falls between the longer and shorter surface 8:1 aspect ratio nozzle PSD_D at most polar angles. The two exceptions where PSD_D does not increase as x_E/H_j increases: (1) the $x_E = 3$" surface at $\theta = 150°$, where the measurement is approaching the dynamic range limit of the separation technique, and (2) the $x_E = 6$" at $\theta = 60°$ where the 16:1 $x_E/H_j = 4.48$ data is very similar to the 8:1 $x_E/H_j = 6$ spectra. In general, the PSD_D spectra from the $x_E = 9$" surface fall closer to the $x_E/H_j = 12$ spectra than might be expected; that is, if linear interpolation were used to predict the the spectra at $x_E/H_j = 6.7$, it would fall much closer to the $x_E/H_j = 6$ line than that of $x_E/H_j = 12$. The difference between the expected behavior and the actual results may be caused by the increase in trailing edge length subject to flow when the nozzle aspect ratio increases and, therefore, related to the nozzle aspect ratio.

Data were acquired at four azimuthal angles with three surfaces: $x_E = 1.3$", $x_E = 6$", and $x_E = 12$". The variation of the JSI noise spectra (PSD_D) with azimuthal angle (ϕ) at setpoint 330 and $\theta = 90°$ (selected as the peak JSI noise relative to the jet mixing noise) is shown in Figure 19. The JSI noise is weak at $x_E = 1.3$" (e.g. Figure 17(a)); as a result the source separation gives spectra for all ϕ that are at the approximate signal-to-noise limit of the source separation technique (Figure 19(a))[h]. The JSI noise source is stronger at $x_E = 6$" (i.e. Figure 17(g)) and PSD_D is consistent with a dipole source, with a maximum at $\phi = 0$ and decreasing at each step to a minimum at $\phi = 90°$ (Figure 19(b)). Finally, at $x_E = 12$" (Figure 19(c)), PSD_D has a higher peak amplitude at $\phi = 0$, $\phi = 30°$, and $\phi = 60°$ than at $x_E = 9$" (Figure 18) but there is less reduction with increasing azimuthal angle; in fact, $PSD_D(\phi = 0)$ is almost the same as $PSD_D(\phi = 30°)$. Thus, it appears that (1) the azimuthal directivity has some sensitivity to surface length and (2) that PSD_D is not a factor at $\phi = 90°$ as the amplitude here is independent of surface. Finally, note that the shedding tone from the septa appears in PSD_D at $\phi = 90°$. Although this tone is not related to the JSI noise source on the aft-deck surface, it is a JSI noise source on the septa trailing edge. Therefore, it shares many properties with PSD_D on the aft-deck and, as a result, is captured by the separation technique in Equation 8.

III.C.5. Surface Effect (G_S)

The surface effect can be computed after PSD_D is extracted from PSD_T using Equation 9. The surface effect term, G_S, is defined as changes to the jet-mixing noise caused by the presence of the surface. There are two primary effects that are captured under this definition: (1) the shielding effect where the surface blocks the jet-mixing noise from reaching the observer and (2) the secondary shear layer effect where the wall-bounded flow passes over the trailing edge and becomes a free-shear flow creating new mixing noise region. These effects can occur at the same time and modify the same frequencies so they may not be separable; for example, a jet-mixing noise source near the nozzle exit is shielded but the small-scale turbulence in the secondary shear layer creates mixing noise at the same frequency cancelling out the shielding effect. In fact, particle image velocimetry (PIV) data has shown that the peak turbulence amplitude in a round jet-surface installation may be found in the secondary shear layer. One hypothesis for this behavior is, unlike at the nozzle exit, there is a more developed free-shear layer on the opposite side of the jet that could drive the mixing in the secondary shear layer to mix more quickly and with higher intensity. In this case, this effect may be more pronounced with a high aspect-ratio nozzle where the opposing shear layer is relatively closer and extends across a longer length. So where the shielding noise could reduce high frequency noise measured by an observer, the secondary shear layer effect could increase this noise.

The third component of G_S is the incoherent portion of the JSI noise source. This part is unrelated to

---

[h] There is no way to know from these data what the actual amplitude of these data below the signal-to-noise limit is and, therefore, they should be removed before attempting to model test results. However, they are shown in these plots for consistency with the other plots.

how the surface modified the jet-mixing noise but is a consequence of the separation method described in Section III.C.3. The method assumes that the JSI noise source (PSD_D) is a coherent point source across its frequency range. If a small length of the surface trailing edge is exposed to the flow, as in a round jet near an offset surface, then the source should be relatively compact and this assumption is reasonable. However, an embedded high aspect-ratio nozzle will generate flow across a longer length of the trailing edge, bringing the validity of this assumption into question. Fortunately, the peak frequency of PSD_D is typically lower than the peak frequency of the jet-mixing noise sources; this provides some ability to separate these effects on visual inspection. However, there is still a cross-over frequency range where PSD_D is decaying that will have a lower signal-to-noise ratio than in an ideal case.

The surface effect at $\phi = 0$, setpoint 330, and $x_E = 3", 6", 12"$ is shown in Figure 20. First, note that the positive values less than $St_{Hj} \approx 0.7$ are due to two factors: (1) the incomplete extraction of PSD_D (compare to Figure 18 to find the overlapping frequency range) and (2) the low frequency effects of the surface. The surface effect at higher Strouhal frequencies depends on the observer angle; at upstream ($\theta = 60°$) and downstream ($\theta = 150°$) angles the amplitude of the effect is relatively small but positive indicating that the surface creates slightly more noise, likely via the secondary shear layer, than it shields while at broadside angles ($90° \leq \theta \leq 120°$) the noise shielding exceeds the noise created. This trend is, at least in part, due to shielding of the broadside noise created near the exit of the isolated 16:1 aspect-ratio nozzle (Figures 11(b)-11(c)); the maximum shielding without this source should occur at upstream angles.

Figure 20 also shows data acquired at a smaller scale factor using an 8:1 aspect ratio nozzle.[10] All data are nondimensionalized using the nozzle slot height to allow a comparison (i.e. surface length is x_E/H_j and Strouhal frequency uses H_j as length-scale) where aspect-ratio is the primary variable. Generally, there is more noise shielding at broadside angles, likely because the 8:1 nozzle did not generate that near-nozzle high frequency noise, and similar results at the upstream angles. At downstream angles, however, the surface effect is similar at $x_E = 3"$ but there are large differences when the surface is longer; there is a surface-flow resonance at $x_E = 6", 9"$ that is captured in the G_S term (see Figures 17(g)-17(j) where these resonances appear as either ridges or as lost data). Similar results are shown in Figures 21 and 22 for setpoints 550 and 770. Note that as the jet velocity increases the difference attributed to surface length become smaller. Also note that G_S falls into a similar trend across aspect-ratio and at downstream angles once the resonance is not present.

The variation of the surface effect (G_S) as a function of azimuthal angle is shown in Figure 23. If the surface were semi-infinite along the major axis then there would be no variation until $\phi \approx 90°$ where the observer would have a direct view of the nozzle. These results show that the surface is not truly infinite but the similarity for $0 \leq \phi \leq 60$ suggest assuming that it is semi-infinite would likely be acceptable. The azimuthal variations, therefore, are more likely driven by changes in PSD_D and PSD_M.

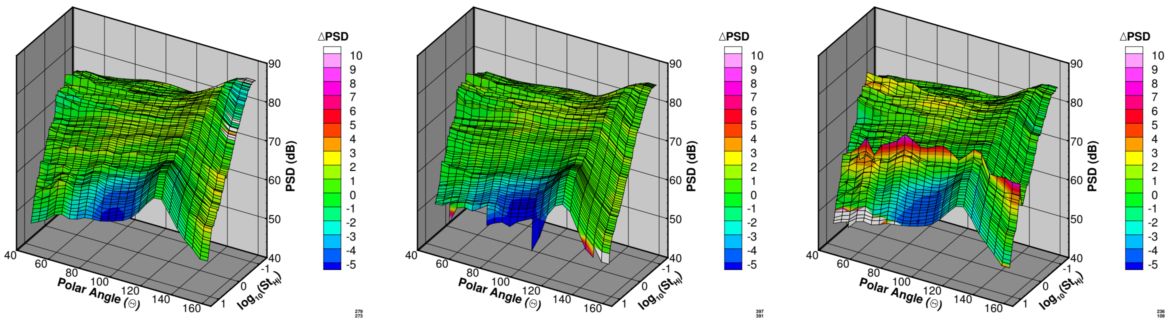

(a) I161

(b) I16A

(c) I16B

Figure 16. Spectra from the the I161, I16A, and I16B septa designs at setpoint 330 and $\phi = 0$ where the spectral shape is from the jet with $x_E = 1.25"$ surface and the color contour is $\Delta PSD = PSD_{surface} - PSD_{isolated}$.

IV. Application to Concept Aircraft

The certification noise metric for new aircraft is the Effective Perceived Noise Level (EPNL) as measured and computed according to the Federal Aviation Regulations - Part 36 (FAR-36) requirements. The FAR-36 procedures require that EPNL is computed using data acquired during a flight test from flyover and sideline

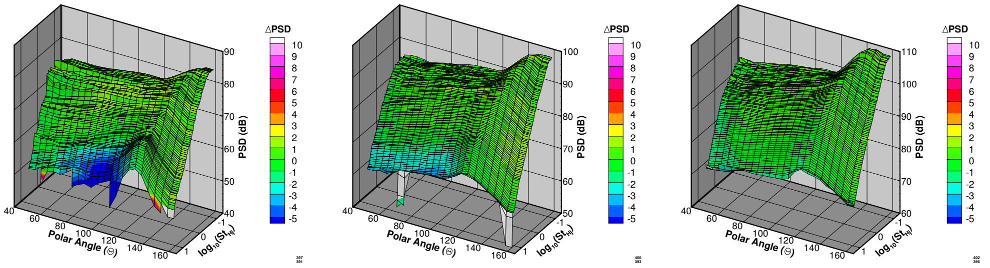

(a) $x_E = 1.25$”, SP 330 (b) $x_E = 1.25$”, SP 550 (c) $x_E = 1.25$”, SP 770

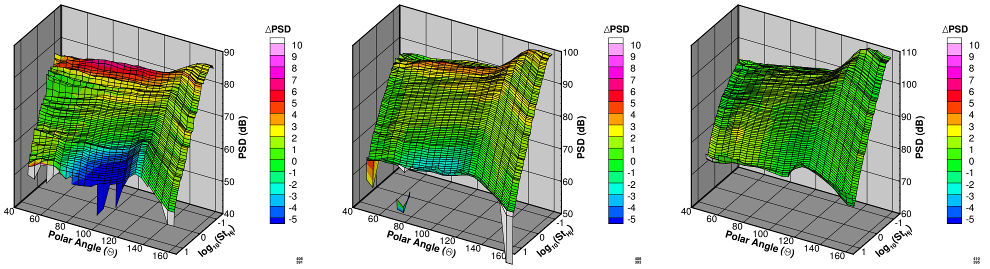

(d) $x_E = 3$”, SP 330 (e) $x_E = 3$”, SP 550 (f) $x_E = 3$”, SP 770

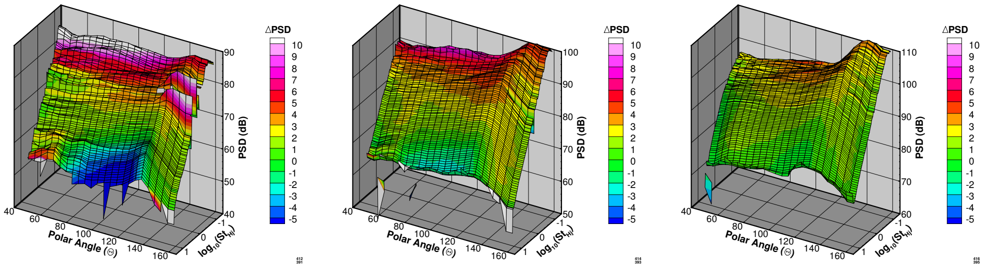

(g) $x_E = 6$”, SP 330 (h) $x_E = 6$”, SP 550 (i) $x_E = 6$”, SP 770

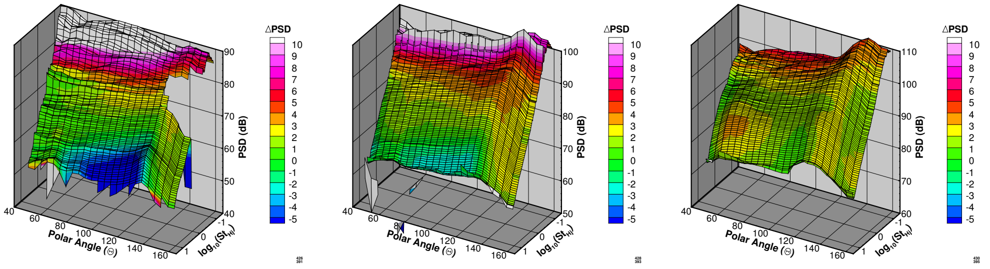

(j) $x_E = 9$”, SP 330 (k) $x_E = 9$”, SP 550 (l) $x_E = 9$”, SP 770

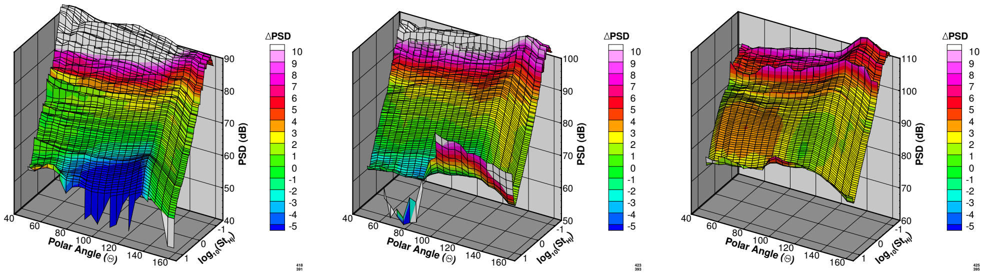

(m) $x_E = 12$”, SP 330 (n) $x_E = 12$”, SP 550 (o) $x_E = 12$”, SP 770

Figure 17. Spectra at $\phi = 0$ for setpoints 330, 550, and 770 for the I16A septa with surfaces $x_E = 1.25”, 3”, 6”, 9”, 12”$ relative to the isolated (no surface) configuration ($\Delta PSD = PSD_{surface} - PSD_{isolated}$).

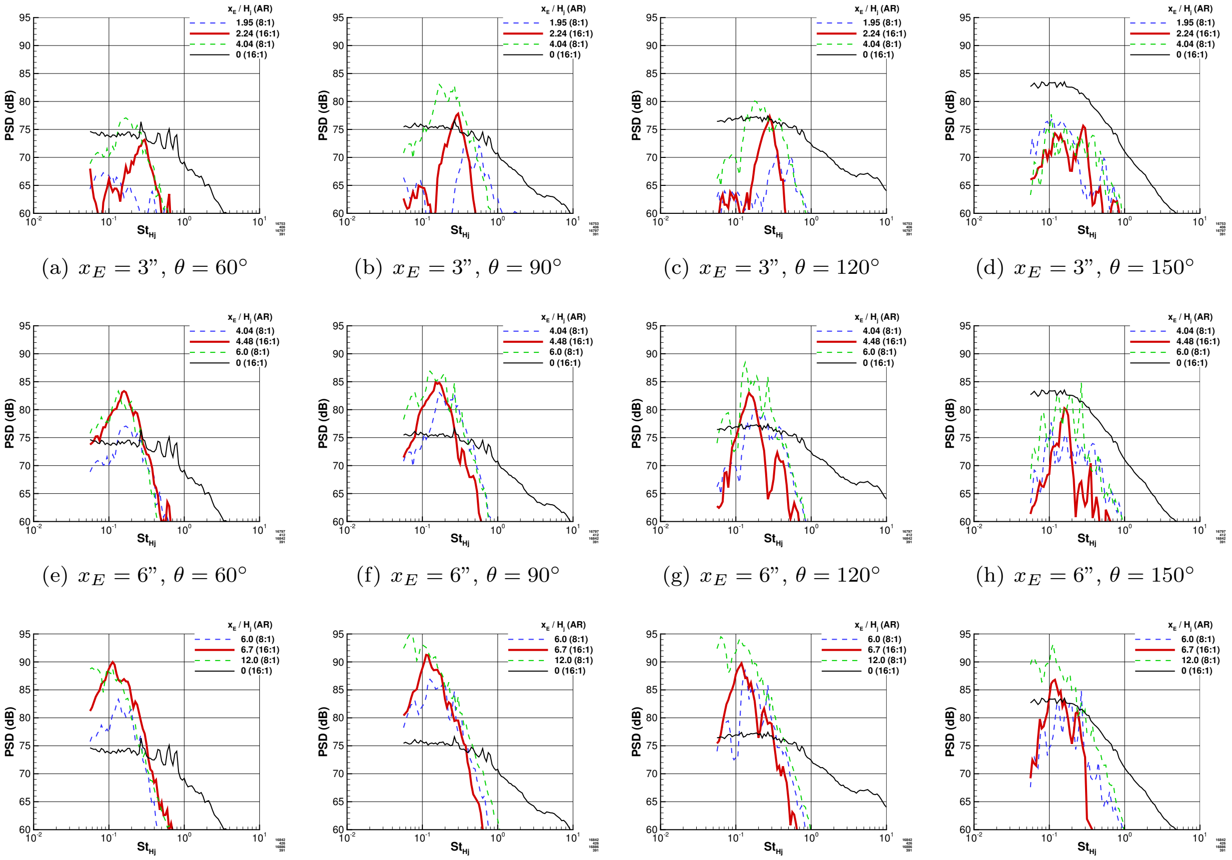

(a) $x_E = 3”$, $\theta = 60°$ (b) $x_E = 3”$, $\theta = 90°$ (c) $x_E = 3”$, $\theta = 120°$ (d) $x_E = 3”$, $\theta = 150°$

(e) $x_E = 6”$, $\theta = 60°$ (f) $x_E = 6”$, $\theta = 90°$ (g) $x_E = 6”$, $\theta = 120°$ (h) $x_E = 6”$, $\theta = 150°$

(i) $x_E = 9”$, $\theta = 60°$ (j) $x_E = 9”$, $\theta = 90°$ (k) $x_E = 9”$, $\theta = 120°$ (l) $x_E = 9”$, $\theta = 150°$

Figure 18. JSI noise source spectra (PSD_D) at $\phi = 0$ and setpoint 330 with the I16A septa near surfaces $x_E = 3”$ and $x_E = 6”$ relative to PSD_M (i.e. $x_E/H_j = 0$). PSD_D acquired from an 8:1 nozzle for similar nondimensional surface lengths is also shown.[10]

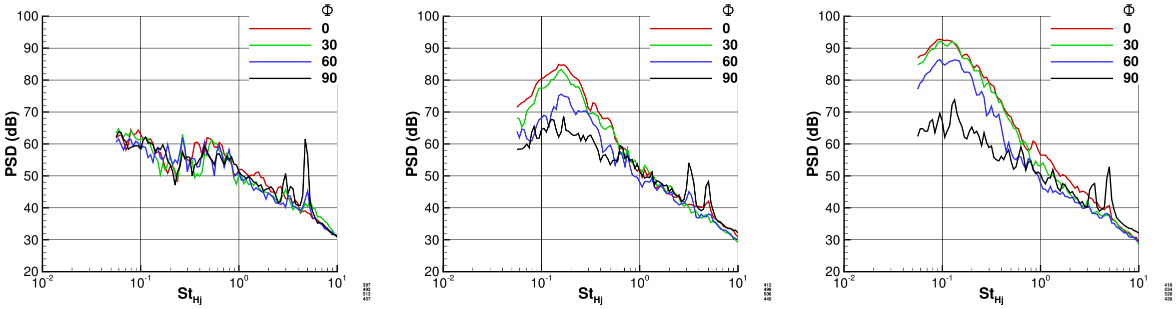

(a) $x_E = 1.3”$ (b) $x_E = 6”$ (c) $x_E = 12”$

Figure 19. Azimuthal variation of the JSI noise (PSD_D) source at setpoint 330 and $\theta = 90°$.

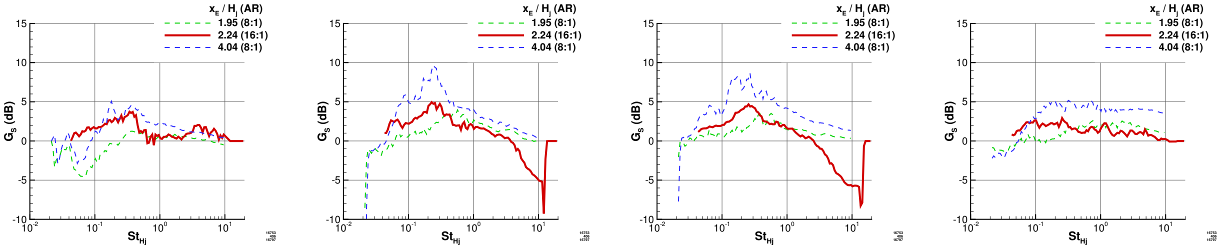

(a) $x_E = 3$”, $\theta = 60°$ (b) $x_E = 3$”, $\theta = 90°$ (c) $x_E = 3$”, $\theta = 120°$ (d) $x_E = 3$”, $\theta = 150°$

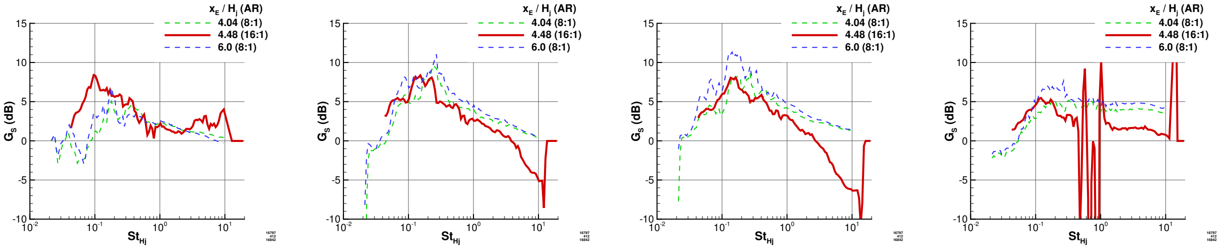

(e) $x_E = 6$”, $\theta = 60°$ (f) $x_E = 6$”, $\theta = 90°$ (g) $x_E = 6$”, $\theta = 120°$ (h) $x_E = 6$”, $\theta = 150°$

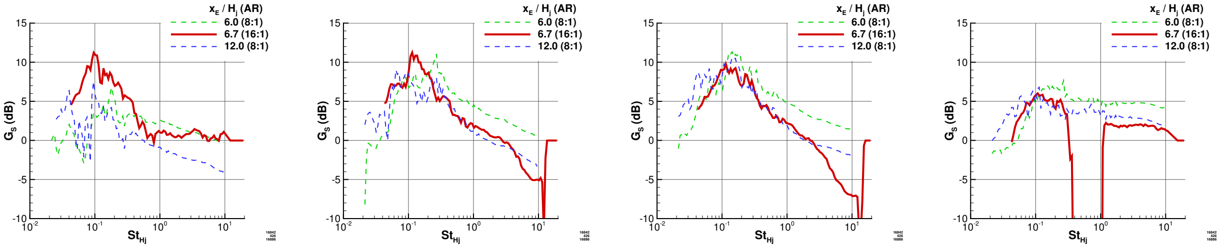

(i) $x_E = 9$”, $\theta = 60°$ (j) $x_E = 9$”, $\theta = 90°$ (k) $x_E = 9$”, $\theta = 120°$ (l) $x_E = 9$”, $\theta = 150°$

Figure 20. JSI noise source spectra (PSD_D) at $\phi = 0$ and setpoint 330 with the I16A septa near surfaces $x_E = 3$” and $x_E = 6$” relative to PSD_M (i.e. $x_E/H_j = 0$). G_S extracted from an 8:1 nozzle for similar nondimensional surface lengths is also shown.[10]

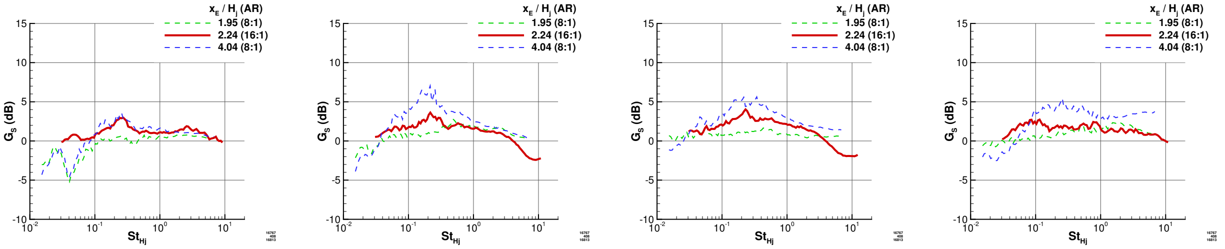

(a) $x_E = 3$", $\theta = 60°$ (b) $x_E = 3$", $\theta = 90°$ (c) $x_E = 3$", $\theta = 120°$ (d) $x_E = 3$", $\theta = 150°$

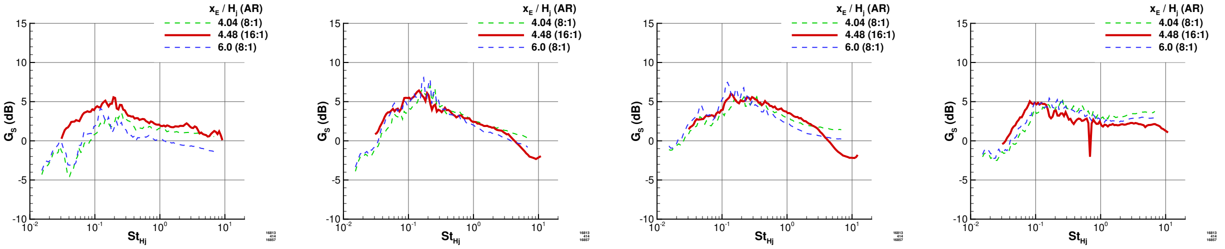

(e) $x_E = 6$", $\theta = 60°$ (f) $x_E = 6$", $\theta = 90°$ (g) $x_E = 6$", $\theta = 120°$ (h) $x_E = 6$", $\theta = 150°$

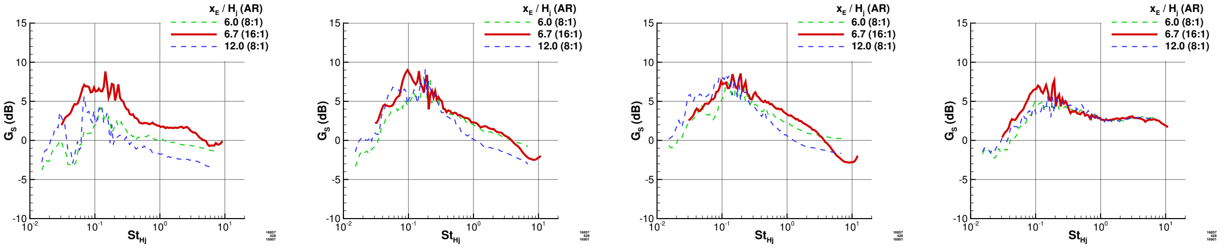

(i) $x_E = 9$", $\theta = 60°$ (j) $x_E = 9$", $\theta = 90°$ (k) $x_E = 9$", $\theta = 120°$ (l) $x_E = 9$", $\theta = 150°$

Figure 21. JSI noise source spectra (PSD_D) at $\phi = 0$ and setpoint 550 with the I16A septa near surfaces $x_E = 3$" and $x_E = 6$" relative to PSD_M (i.e. $x_E/H_j = 0$). G_S extracted from an 8:1 nozzle for similar nondimensional surface lengths is also shown.[10]

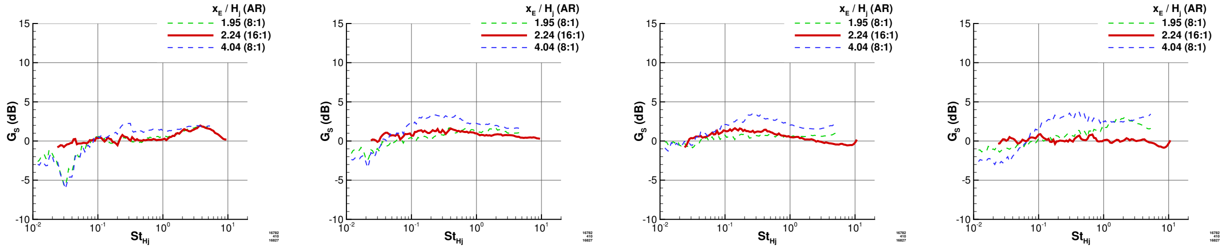

(a) $x_E = 3$”, $\theta = 60°$ (b) $x_E = 3$”, $\theta = 90°$ (c) $x_E = 3$”, $\theta = 120°$ (d) $x_E = 3$”, $\theta = 150°$

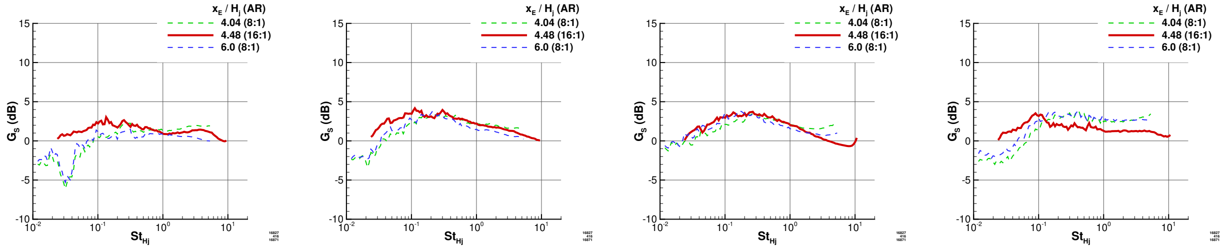

(e) $x_E = 6$”, $\theta = 60°$ (f) $x_E = 6$”, $\theta = 90°$ (g) $x_E = 6$”, $\theta = 120°$ (h) $x_E = 6$”, $\theta = 150°$

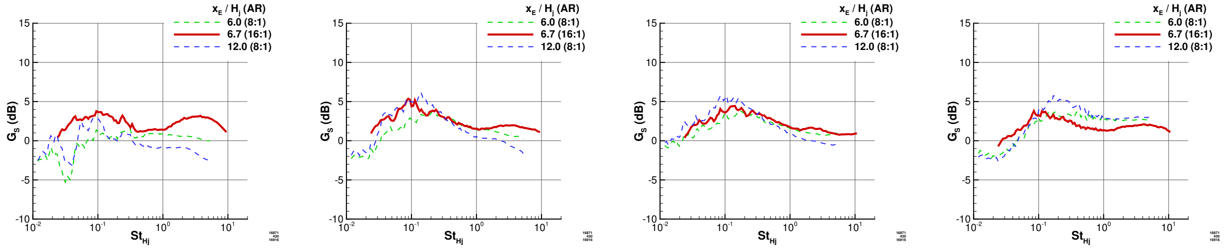

(i) $x_E = 9$”, $\theta = 60°$ (j) $x_E = 9$”, $\theta = 90°$ (k) $x_E = 9$”, $\theta = 120°$ (l) $x_E = 9$”, $\theta = 150°$

Figure 22. JSI noise source spectra (PSD_D) at $\phi = 0$ and setpoint 770 with the I16A septa near surfaces $x_E = 3$” and $x_E = 6$” relative to PSD_M (i.e. $x_E/H_j = 0$). G_S extracted from an 8:1 nozzle for similar nondimensional surface lengths is also shown.[10]

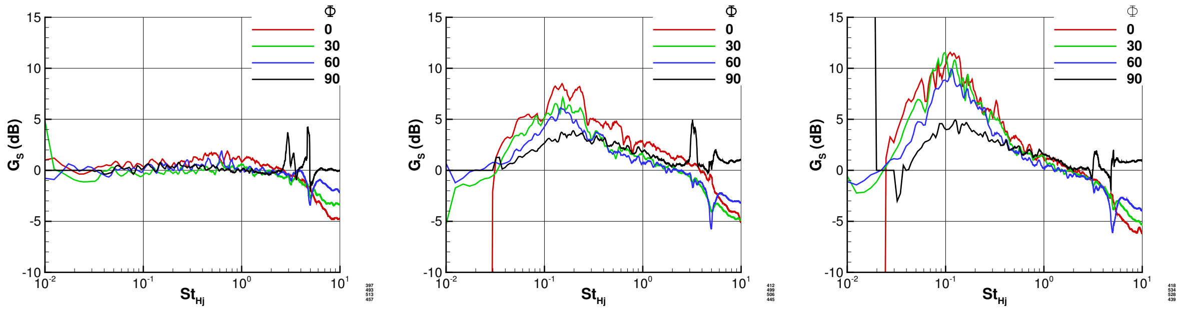

(a) $x_E = 1.3$” (b) $x_E = 6$” (c) $x_E = 12$”

Figure 23. Azimuthal variation of the JSI noise (PSD_D) source at setpoint 330 and $\theta = 90°$.

microphone arrays that is transformed to 1/3-octave spectra, weighted on a frequency-by-frequency basis for the human hearing response, and integrated over frequency and exposure time to get one number, in EPNdB, for the sideline, takeoff, and approach observer locations. Projecting EPNL using scale-model data requires adjusting the frequency and amplitude to reflect the increase in size and post-processing the data to an assumed flight altitude and speed; depending on the polar and azimuthal observer angles acquired, the data may or may not be suitable for variable altitude takeoff / landing profile. Therefore, the analysis that follows is based on (1) projection to a Mach 0.3 level flight profile at 850 ft altitude [i] and (2) will focus on changes in EPNL as different parameters are varied rather than projecting the absolute number that would be measured in a flight test.

Scale-model tests are often used during the early design phase of a project to identify potential problems and select the best ideas from a range of possible concepts. The Jet-Surface Interaction - High Aspect Ratio Nozzle test was inspired by the propulsion system on the N3-X concept aircraft: an approximately 32:1 aspect ratio integrated distributed exhaust slot nozzle with an aft airframe deck. This concept posed several problems at model-scale but the most relevant for transformation to full-scale are that (1) the aspect-ratio and (2) nozzle height were limited by the size of the jet rig and its maximum flow rate. The effect of nozzle aspect-ratio was investigated in Section III.C using comparisons with an 8:1 aspect-ratio nozzle and examining the trends. The nozzle height (H_j) is key scaling factor for frequency and, therefore, the critical factor in the EPNL calculation. The slot height of the N3-X distributed exhaust ($H_{j,full-scale}$) may vary based on fan pressure ratio (FPR) to maximize efficiency and is estimated between 22" and 24.5" for $1.3 \leq FPR \leq 1.35$ using data from Reference [4]. The general rule is that frequency scales linearly with the H_j so that scale-factor is $S_f = H_{j,full-scale}/H_{j,model-scale}$; taking $H_{j,full-scale} = 22$" with $H_{j,model-scale} = 1.34$" (septa I16A) gives data through the 5 kHz 1/3-octave band for all setpoints / configurations. Ideally the EPNL would be calculated using all bands up to 10 kHz but this more limited range will at least include the critical 2-4 kHz bands. Therefore, EPNL will be calculated using $H_{j,full-scale} = 22$".

The EPNL for each combination of setpoint and surface length was computed assuming a level flyover at 850-ft. altitude, Mach 0.3 flight speed, and $H_{j,full-scale} = 22$". The results for the flyover ($\phi = 0$) observer are shown in Table 5. These data show that surfaces may reduce the EPNL for low jet velocities most likely to correspond to an approach throttle setting (i.e. setpoints 330-440). However, at jet velocities corresponding to cruise and takeoff settings (i.e. setpoints 550-770) where engine noise is a more significant factor, the shortest surface has minimal impact on the EPNL and the longer surfaces increase the EPNL versus the isolated jet.

Figure 24 shows the the annoyance weightings as a function of frequency and exposure time (t_e). The peak annoyance in the isolated ($x_E = 0$) jets is around 2 kHz for exposure times (t_e) between 0 and 4 seconds. Human hearing is particularly sensitive to sound in the 2 kHz range so an annoyance penalty is expected on any significant noise around this frequency. There is a second region of annoyance around the $f = 316$ Hz 1/3-octave band at setpoints 550 and 770. The annoyance weightings of the installed jet diverge based on jet velocity, with setpoint 330-440 on one end and setpoints 550-770 on the other. At setpoint 330, for example, the surface shields the observer from the annoying 2 kHz noise source at broadside angles (24, Left) to reduce the EPNL; this shielding was found in the surface effect G_S functions (Section III.C.5, e.g. Figure 20) and is, in part, shielding of the noise increase found at setpoint 330 in the isolated jet (Figures 11(b)-11(c)). Similarly, there is some shielding of the 2 kHz frequency band at setpoint 550 but it is not as effective and requires a much longer surface (e.g. compare Figures 24(b) and 24(q)). Unlike setpoint 330, the annoyance weightings at setpoints 550 and 770 have a second peak around 316 Hz that increases in size (frequency range and duration) with surface length. The peak of the JSI noise spectrum is $90Hz \leq f \leq 160Hz$, depending on jet velocity; this frequency range is too low for this noise to merit a high annoyance weight. Rather the 316 Hz peak appears where the JSI noise peak is decaying and near the level of the jet-mixing noise. The surface effect (G_S) in this frequency range levels out to a positive value indicating that the surface is creating more noise than it is shielding. As discussed in Section III.C.4, a new free-shear layer develops at the surface trailing edge and flow data from round jets has shown that the peak turbulent kinetic energy for the entire system can appear in this developing shear layer. The rectangular jet provides ideal conditions for a dynamic shear layer by (1) increasing the trailing edge length exposed to flow and (2) providing a developed shear layer in close proximity (i.e. the non-surface side) that might drive its development. It is, therefore, this effect rather than the JSI dipole noise that creates the increased EPNL when scale-factor is fully considered. Furthermore, the shear layer that develops from the surface trailing edge is, by definition, not subject to

---

[i] The 850 foot altitude was selected so that $\phi = 60°$ corresponds to the 1476 ft sideline distance used Reference [5]

any surface shielding effect so the impact on EPNL is found at other azimuthal angles where the JSI trailing edge dipole is reduced by its natural directivity (Tables 6-7). Ultimately these data suggest that, perhaps counterintuitively, longer surfaces near an embedded high-aspect ratio tend to create more noise than using shorter or no surfaces.

Setpoint	$x_E = 0$	$x_E = 1.25$”	$x_E = 3$”	$x_E = 6$”	$x_E = 9$”	$x_E = 12$”
330	81.7	80.5	80.7	81.6	80.5	80.4
440	86.6	85.8	86.6	87.5	87.0	86.7
550	91.6	91.2	92.2	93.2	93.4	93.0
660	96.8	96.3	97.1	98.0	98.4	98.7
770	101.4	101.3	101.9	102.9	103.7	104.6

Table 5. EPNL calculated for the direct flyover microphone array ($\phi = 0$) using a Mach 0.3 flight speed, level 850 ft. flight altitude, and $H_{j,full-scale} = 22$” nozzle exit height. Note that $x_E = 0$ is the isolated (no surface) configuration.

Setpoint	$x_E = 0$	$x_E = 1.25$”	$x_E = 6$”	$x_E = 12$”
330	81.0	80.3	79.9	80.2
440	86.2	85.9	86.1	86.6
550	91.3	91.2	92.0	92.5
660	96.2	96.6	97.1	99.0
770	101.0	101.0	102.1	105.8

Table 6. EPNL calculated for the direct flyover microphone array ($\phi = 30°$) using a Mach 0.3 flight speed, level 850 ft. flight altitude, and $H_{j,full-scale} = 22$” nozzle exit height. Note that $x_E = 0$ is the isolated (no surface) configuration.

Setpoint	$x_E = 0$	$x_E = 1.25$”	$x_E = 6$”	$x_E = 12$”
330	79.2	79.1	78.8	78.8
440	84.7	84.2	85.1	85.2
550	89.8	89.6	90.5	90.8
660	94.6	94.5	95.6	96.0
770	99.0	99.3	100.4	103.3

Table 7. EPNL calculated for the direct flyover microphone array ($\phi = 60°$) using a Mach 0.3 flight speed, level 850 ft. flight altitude, and $H_{j,full-scale} = 22$” nozzle exit height. Note that $x_E = 0$ is the isolated (no surface) configuration.

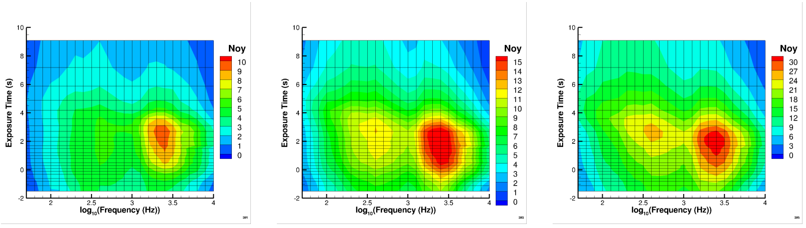

(a) SP 330, $x_E = 0$” (b) SP 550, $x_E = 0$” (c) SP 770, $x_E = 0$”

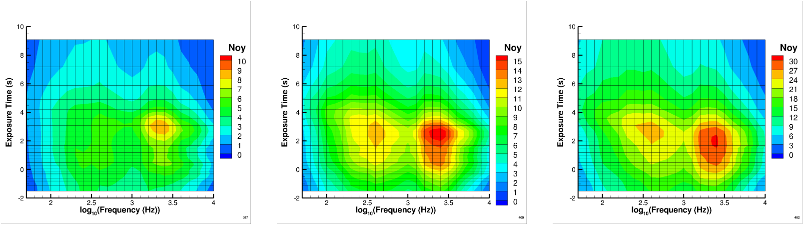

(d) SP 330, $x_E = 1.25$” (e) SP 550, $x_E = 1.25$” (f) SP 770, $x_E = 1.25$”

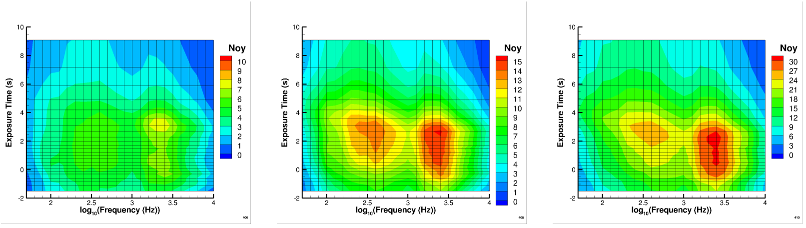

(g) SP 330, $x_E = 3$” (h) SP 550, $x_E = 3$” (i) SP 770, $x_E = 3$”

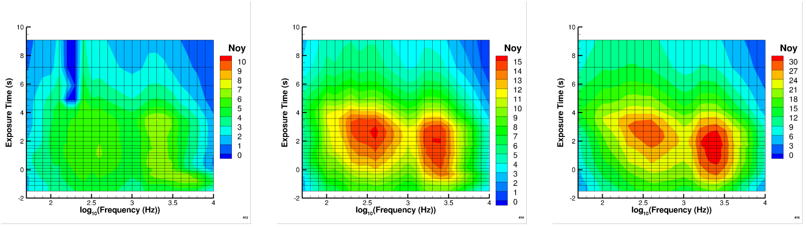

(j) SP 330, $x_E = 6$” (k) SP 550, $x_E = 6$” (l) SP 770, $x_E = 3$”

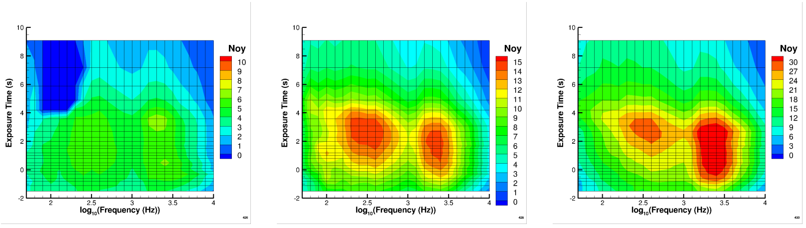

(m) SP 330, $x_E = 9$” (n) SP 550, $x_E = 9$” (o) SP 770, $x_E = 9$”

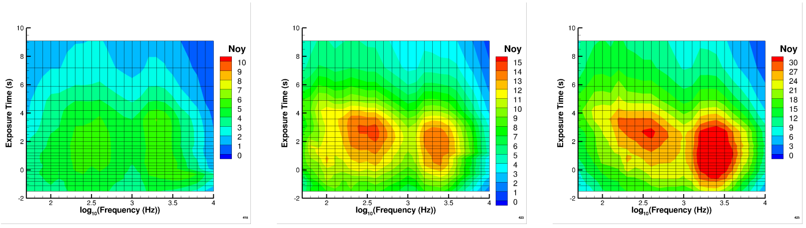

(p) SP 330, $x_E = 12$” (q) SP 550, $x_E = 12$” (r) SP 770, $x_E = 12$”

Figure 24. Annoyance values from the flyover ($\phi = 0$) microphone array for setponts 330, 550, and 770. Note (1) that the scale changes as septoint increases and (2) that the surface lengths correspond to model-scale to facilitate comparison with other sections.

V. Conclusions

Far-field, phased-array noise source localization, and in-flow pressure data have been acquired using a 16:1 aspect-ratio nozzle with various septa and flush mounted surfaces inspired by the NASA N3-X concept aircraft. The in-flow pressure data verified that the nozzle, designed using CFD to transition from the circular cross-section of the jet rig to the rectangular cross-section at the nozzle exit, provided an acceptable flow profile. These data were also used to calculate the jet potential core length, an important parameter for jet-surface interaction (JSI) noise modeling; it approximately follows the scaling developed for round single stream jets but with the slot height rather than exit diameter as the critical length scale. Phased-array noise source localization data showed some differences between the nozzle septa designs, most notably the frequency where the peak noise source jumped from the jet plume to the septa trailing edge at the nozzle exit. Far-field noise data were compared with data previously acquired using lower aspect-ratio rectangular nozzles to show some inconsistency in the uninstalled jet-mixing noise at high Strouhal frequencies with the 16:1 aspect-ratio nozzle; however, there is not enough data to make any firm conclusion to the source of this change. Far-field noise data acquired with simple aft deck surfaces of varying length showed (1) significant JSI dipole noise source at the trailing edge, (2) some noise shielding at lower flow velocities, and (3) increased noise at higher Strouhal numbers for high jet velocities. Finally, these model-scale far-field noise data were transformed to simulate the full-scale flyover EPNL of an N3-X like propulsion system with an aft deck airframe surface. The EPNL and annoyance weightings show that the aft deck surface reduces the the EPNL at lower jet velocities, likely corresponding to approach engine settings, compared to the isolated jet, and increases the EPNL at the higher jet velocities more likely at takeoff and cruise engine settings. These data, combined with past experimental results, suggest that the secondary shear layer formed at the surface trailing edge may be responsible for a significant part of the noise increase. This effect is stronger in higher aspect-ratio nozzles because more of the surface trailing edge is exposed to flow and the opposite free-shear layer is relatively closer and, therefore, capable of increasing the turbulence intensity in the new shear-layer. Longer surface lengths also tend to create more noise than isolated jets or jets near shorter surfaces, an indication that simply adding surface length to shield more of the jet-mixing noise sources would be problematic. The secondary shear-layer effect may be somewhat mitigated by the flight effect, which reduces the shear-layer strength between the jet and ambient, or by changing the shape or material of the aft deck surfaces but these factors were not considered in this test.

Acknowledgements

The authors would like to thank Paul Gebby and Dale Robinson of Vantage Partners for the structural analysis of the hardware tested, the staff at the NASA Glenn Research Center Aero-Acoustic Propulsion Laboratory for their work executing the test, and Dr. James Bridges and Dr. Khairul Zaman for reviewing this manuscript.This work was supported by the NASA Advanced Air Vehicle Program, Advanced Air Transportation Technologies Project.

References

[1] Jameson, K. K., Marshall, D. D., Ehrmann, R., Lichtwardt, J. A., Paciano, E. N., Englar, R. J., Horne, W. C., "Cal Polys AMELIA 10 Foot Span Hybrid Wing-Body Low Noise CESTOL Aircraft Wing Tunnel Test and Experimental Results Overview", AIAA 2013-0974, 2013.

[2] Gou, Y., Burley, C. L., Thomas, R. H., "On Noise Assessment for Blended Wing Body Aircraft", AIAA 2014-0365.

[3] Kim, H., Liou, M.-F., Liou, M.-S., "Mail-Slot Nacelle Shape Design for N3-X Hybrid Wing-Body Configuration", AIAA 2015-3805, 2015.

[4] Felder, J.L., Kim, H.-D., Brown, G., Chu, J., "An Examination of the Effect of Boundary Layer Ingestion on Turboelectric Distributed Propulsion Systems", AIAA 2011-0300, 2011.

[5] Berton, J. J., Haller, W. J., "A Noise and Emissions Assessment for the N3-X Transport", AIAA 2014-0594, 2014.

[6] , Brown, C., "Jet-Surface Interaction Test: Far-Field Noise Results", ASME GT2012-69639, 2012.

[7] Brown, C.A. , "Jet-Surface Interaction Test: Far-Field Noise Results", J. Eng. Gas Turbines Power, **1**35(7), Jun. 2013.

[8] Podboy, G., "Jet-Surface Interaction Test: Phased Array Noise Source Localization Results", ASME GT2012-69801, 2012.

[9] Brown, C., "Including Finite Surface Span Effects in Empirical Jet-Surface Interaction Noise Models", AIAA 2016-0006, 2016.

[10] Bridges, J., "Noise from Aft Deck Exhaust Nozzles - Differences in Experimental Embodiments", AIAA 2014-0876, 2014.

[11] Bridges, J., ”Measurements of Turbulent Flow Field in Separate Flow Nozzles with Enhanced Mixing Devices - Test Report”, NASA/TM-2002-211366, 2002.

[12] Brown, C., Henderson, B., Bridges, J., ”Data Quality Assurance for Supersonic Jet Noise Measurements”, Proc. ASME Turbo Expo 2010, GT2010-22545, 2010.

[13] Dippold III, V. F., ”Design and Analysis of High Aspect Ratio Nozzles for Distributed Propulsion Acoustic Measurements”, AIAA 2016-3876, 2016.

[14] Bridges, J., ”Simple Scaling Of Multi-Stream Jet Plumes For Aeroacoustic Modeling”, AIAA 2016-1637, 2016.

[15] Bridges, J., Wernet, M.P., ”The NASA Subsonic Jet Particle Image Velocimetry (PIV) Dataset”, NASA/TM- 2011-216807, 2011.

[16] Bridges, J. and Brown, C., ”Validation of the Small Hot Jet Acoustic Rig for Jet Noise Research”, AIAA 2005-2846, 2005.

[17] Brown, C. and Bridges, J., ”Small Hot Jet Acoustic Rig Validation”, NASA/TM-2006-214324, 2006.

[18] Zaman, K. B. M. Q., Fagan, A. F., Bridges, J. E., and Brown, C. A., ”An experimental investigation of resonant interaction of a rectangular jet with a flat plate”, J. of Fluid Mech., vol. 779, pp. 751-775, 2015.

[19] Brown, C., ”An Empirical Jet-Surface Interaction Noise Model with Temperature and Nozzle Aspect Ratio Effects”, AIAA 2015-0229, 2015.

[20] Brown, C., Podboy, G., Bridges, J., ”Modeling Jet-Surface Interaction Noise for Separate Flow Nozzles”, AIAA 2016-2862, 2016.

[21] Frate, F., Bridges, J., ”Extensible Rectangular Nozzle System”, AIAA 2011-0975, 2011.

[22] Brown, C., ”An Empirical Jet-Surface Interaction Noise Model with Temperature and Nozzle Aspect Ratio Effects”, AIAA 2015-0229, 2015.

[23] Zaman, K. B. M. Q., Bridges, J., Brown, C., ”Excess Broadband Noise Observed with Overexpanded Jets”, AIAA J., 48(1), pp. 202-214, 2010.

[24] Zaman, K. B. M. Q., Bridges, J. E., Fagan, A. F., Brown, C. A., ”An experimental investigation of jet noise from septa nozzles”, AIAA 2016-2991, 2016.

[25] Brown, C., ”Developing an Empirical Model for Jet-Surface Interaction Noise”, AIAA 2014-0878, 2014.

[26] Brown, C., Wernet, M., ”Jet-Surface Interaction Test: Flow Measurement Results”, AIAA 2014-3198, 2014.

[27] Brown, C., ”Empirical Models for the Shielding and Reflection of Jet Mixing Noise by a Surface”, AIAA 2015-3128, 2015.